CrossMark

J. Fluid Mech. (2021), *vol*. 907, A33. © The Author(s), 2020.
Published by Cambridge University Press
doi:10.1017/jfm.2020.842

Cylindrical rotating Rayleigh–Taylor instability

M. M. Scase[1,2,†] **and S. Sengupta**[1,3]

[1]Geophysical Fluid Dynamics, Woods Hole Oceanographic Institution, Woods Hole, MA 02543, USA
[2]School of Mathematical Sciences, University of Nottingham, Nottingham NG7 2RD, UK
[3]NERSC, Lawrence Berkeley National Laboratory, 1 Cyclotron Road, Berkeley, CA 94720, USA

(Received 27 February 2020; revised 13 August 2020; accepted 30 September 2020)

We consider a spun-up system of an inner cylinder of fluid surrounded by an outer fluid layer within a rotating cylindrical container, in the absence of gravity. The outer layer may be of differing density and viscosity to the inner layer. If the inner layer is denser than the outer layer then the effect of rotation, in the presence of a perturbation to the interface between the two layers, is to force the inner fluid outwards and the outer fluid inwards, subject to possible surface tension stabilisation. The relative importance of viscosity to rotation is described by an Ekman number. We investigate the behaviour of perturbations to the interface in the inviscid limit and low and high viscosity limits. In the low viscosity limit, perturbations grow as an $O(Ek^{1/2})$ correction to the inviscid growth rate. In the high viscosity limit, perturbations grow as $O(Ek^{-1})$. In the absence of surface tension, the preferred mode of growth is independent of the layer density difference and depends only upon the domain aspect ratio, initial position of the interface, and viscosity contrast. Numerical simulations of the flow are carried out using a volume-of-fluid formulation. The growth rates from these simulations are compared with the theoretical predictions in both low and high viscosity limits and the agreement is seen to be good. Finally, we examine the special case of a single-layer rotating viscous column and describe the preferred-mode boundary between a varicose mode and a spiral mode in the high viscosity, high surface tension limit.

Key words: rotating flows, multiphase flow

1. Introduction

The Rayleigh–Taylor instability (Rayleigh 1883; Taylor 1950) has received sustained research interest over the past century. Many natural occurrences of the flow have been discovered and the uses and applications of the instability have been increasingly exploited (see Zhou (2017*a*,*b*) for a comprehensive recent review of the subject, or for example Boffetta & Mazzino (2017)). The original work of Rayleigh considered the instability due to heavier fluid overlaying lighter fluid in both cases of either a continuous or a step density stratification. In 1950 Taylor showed that the instability due to a heavy uniform layer overlying a light uniform layer under the action of gravity was identical to that of a stable two-layer stratification being accelerated vertically downwards at a rate greater than gravity. The initial linear growth rate is determined by the wavelength of a given

† Email address for correspondence: matthew.scase@nottingham.ac.uk

https://doi.org/10.1017/jfm.2020.842 Published online by Cambridge University Press

perturbation, the effective gravitational acceleration that the system experiences and the density contrast between the two fluids. The growth rate may be further affected by fluid viscosity and surface tension between the fluid layers. To some extent these fluid properties are set by the situation in which the instability is occurring and there may not be a way for these properties to be manipulated if the intention is to influence the instability in some beneficial way. As such, investigators have sought to understand the influence of long-range effects, including rotation and magnetic fields on the instability (see e.g. Chandrasekhar 1961). A further motivation for such study is that the presence of strong rotation and magnetic fields in astrophysical scale flows is commonly understood to occur. Previous studies have considered rotation perpendicular or parallel to a density stratification (e.g. Dávalos-Orozco 1993; Carnevale *et al.* 2002; Tao *et al.* 2013) or more general rotation of the system (e.g. Dávalos-Orozco & Aguilar-Rosas 1989*a*,*b*; Dávalos-Orozco 1996*a*,*b*). As these studies have been often motivated by astrophysical applications (e.g. García-Senz, Cabezon & Domínguez 2018) the influence of viscosity on the development of the instability has not necessarily been considered, though investigations have been conducted into the global stability of rotating viscous systems (e.g. Joseph *et al.* 1985). Here our emphasis is on the effects of viscosity on the growth rate of the three-dimensional rotating Rayleigh–Taylor instability in a cylindrical domain with an initially cylindrical interface between the two fluids that may support surface tension effects.

Recent work has considered the effect of rotation on the Rayleigh–Taylor instability both experimentally (Baldwin, Scase & Hill 2015; Scase, Baldwin & Hill 2017*a*, 2020) and theoretically (Scase, Baldwin & Hill 2017*b*) in the low rotation rate limit focussing on the importance of the initial hydrostatic state. This work builds upon previous studies by Chandrasekhar (1961) and Miles (1964). Chandrasekhar considered the effect of rotation on a two-layer unstable stratification with an initially planar interface. However, Miles showed that the frequency of free-surface oscillations predicted by Lamb (1932) on a body of rotating liquid were in error, due to the assumption of a planar free-surface, by the same order of magnitude as the correction for rotation. In Scase & Hill (2018) the authors consider the high rotation limit of the Rayleigh–Taylor instability in inviscid and viscous configurations and investigate the effects of surface tension and interfacial diffusion. However, this study was strictly two-dimensional, considering only azimuthal perturbations to two fluid layers confined in a circular domain; the effect of axial perturbations was necessarily neglected. Here we extend that study to three dimensions.

We consider an inner cylindrical column of fluid surrounded by an outer fluid layer all within a cylindrical container (unlike Weidman, Goto & Fridberg (1997) and Dávalos-Orozco & Vázquez-Luis (2003), we do not consider the case of a solid inner cylinder such as in a Taylor–Couette configuration). The outer fluid may differ from the inner fluid both in density and viscosity. The fluids are considered initially to be 'spun-up' into solid-body rotation (there is no initial shear between the fluid layers unlike one of the cases considered by Hocking & Michael (1959)). We further allow for the possibility that there may also be surface tension between the two fluid layers. We consider the system as the extreme high rotation rate limit of the rotating Rayleigh–Taylor instability, where the influence of gravity may be neglected; it may be considered as a fully three-dimensional fluid–fluid centrifuge for cases where a Hele-Shaw approximation is not appropriate. The set-up is illustrated in figure 1 for an axial wavenumber $n = 10$ and azimuthal wavenumber $m = 12$. By considering the system in the limits of high and low viscosity we are able to show the dependence of the growth rate on the Ekman number, Ek, that characterises the relative importance of viscosity to rotation. When the system is in the low viscosity regime, $Ek \ll 1$, the effect of viscosity is to modify the inviscid growth rate by an order $Ek^{1/2}$

https://doi.org/10.1017/jfm.2020.842 Published online by Cambridge University Press

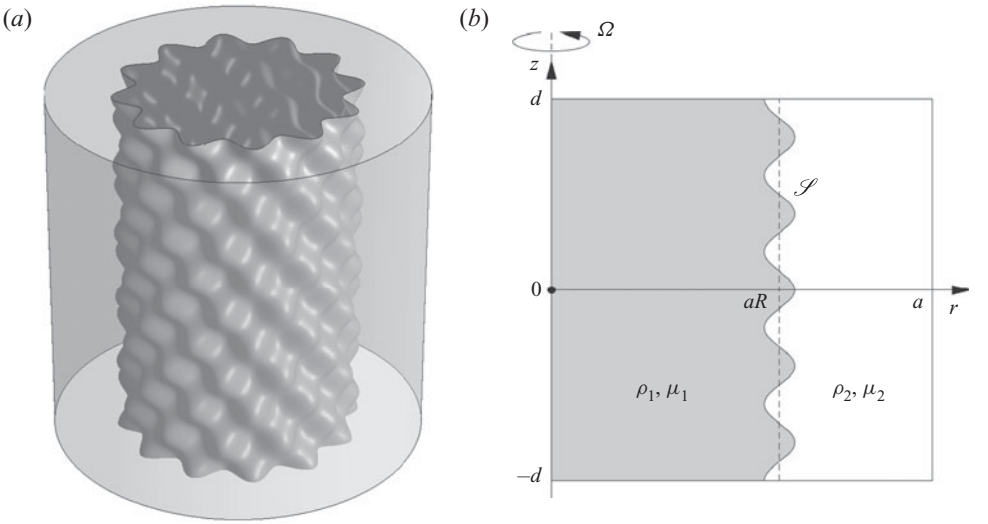


FIGURE 1. (*a*) The initial perturbation for axial wavenumber $n = 10$ and azimuthal wavenumber $m = 12$. If the inner fluid layer is denser than the outer the perturbation on the interface will grow as the two fluids move in opposite radial directions. (*b*) Schematic of the meridional plane. Quantities associated with the inner layer have subscript 1, quantities associated with the outer layer have subscript 2. The interface, $\mathscr{S}$, is a perturbation about $r = aR$ (using dimensional quantities).

correction that we derive. Conversely, when the system is in the high viscosity regime, $Ek \gg 1$, the instability growth rate behaves as Ek^{-1}. The effect of surface tension in the unstable configuration is to suppress the growth rate and possibly completely stabilise otherwise unstable modes of instability. The effect is greatest upon perturbations with the shortest wavelengths.

A special case of the flow configuration investigated is that of a rotating viscous column of fluid. In § 4 we examine this limit by allowing the density and viscosity of the outer fluid layer to tend to zero. Important applications of this flow are discussed in Kubitschek & Weidman (2007*a*) together with a linear stability analysis. As part of their extensive study, Kubitschek & Weidman (2007*a*) considered which mode of instability has the greatest growth rate in the limit of high viscosity and high surface tension. They established that in this region the two most unstable modes are an axisymmetric 'varicose' mode and a 'spiral' mode. Their numerical results suggested that there is an asymptotic form of the boundary at which the preferred mode of instability switches from varicose to spiral. We are able to derive and confirm their conjectured form of this boundary.

Though our flow configuration is idealised, it provides a connection between practical, realisable flows including, amongst others, stable coating flows on the inside of cylinders (e.g. Johnson 1988) with applications in turbojet engine cooling (e.g. Chew 1996), unstable liquid atomisation and combustion flows (discussed in Kubitschek & Weidman (2007*a*)) and liquid jet instability in fusion processes (e.g. Chen, Schrock & Peterson 1997).

The layout of the paper is as follows. In § 2 we introduce the governing model and the required boundary conditions and matching conditions at the interface between the two fluids. We first find a dispersion relation for the development of the instability for two inviscid fluid layers that may have surface tension acting between them. We then develop the inviscid solution by considering an asymptotic correction for the case of weakly

https://doi.org/10.1017/jfm.2020.842 Published online by Cambridge University Press

viscous fluid layers. We next consider the case of highly viscous fluid layers and derive an expression for the growth rate in the case of equal viscosity in each layer (the full solution for highly viscous fluids with a viscous contrast is given in appendix B). In § 3 we show the results of numerical simulations of the instability in both high and low viscosity cases and compare the observed growth rates of the simulations with the theoretical predictions of § 2 and show that they are in good agreement. In § 4 we investigate the special limiting case of a rotating viscous column. Finally, in § 5 we draw our conclusions.

2. Modelling

We consider two layers of uniform density and uniform viscosity fluid arranged as concentric cylinders. The equations of motion for the fluid velocity $\boldsymbol{u}_i$ and pressure p_i, in each layer $i = 1$ (inner) and $i = 2$ (outer) are the rotating Navier–Stokes equations with incompressibility given by

$$\rho_i \frac{\mathrm{D}\boldsymbol{u}_i}{\mathrm{D}t} = -\boldsymbol{\nabla} p_i - \rho_i \boldsymbol{\Omega} \times (\boldsymbol{\Omega} \times \boldsymbol{x}) - 2\rho_i \boldsymbol{\Omega} \times \boldsymbol{u}_i + \mu_i \nabla^2 \boldsymbol{u}_i, \tag{2.1a}$$

$$\boldsymbol{\nabla} \cdot \boldsymbol{u}_i = 0. \tag{2.1b}$$

We work in cylindrical polar coordinates with unit basis vectors $\hat{\boldsymbol{r}}$, $\hat{\boldsymbol{\theta}}$ and $\hat{\boldsymbol{z}}$ in the radial, azimuthal and axial directions, respectively. Here $\boldsymbol{\Omega}$ is the rotation vector, taken without loss of generality to be $\boldsymbol{\Omega} = \Omega\,\hat{\boldsymbol{z}}$. Following Scase & Hill (2018) we non-dimensionalise time by Ω^{-1}, and length by the radial extent of the domain a (see figure 1). The density and viscosity in each layer is non-dimensionalised as in Scase & Hill (2018) using a system mean density $\rho_0 = (\rho_1 + \rho_2)/2$ and system mean viscosity $\mu_0 = (\mu_1 + \mu_2)/2$. Hence we have that

$$\frac{\mathrm{D}\boldsymbol{u}_i}{\mathrm{D}t} = -\frac{1}{\rho_i}\boldsymbol{\nabla} p_i + r\,\hat{\boldsymbol{r}} - 2\hat{\boldsymbol{z}} \times \boldsymbol{u}_i + Ek\frac{\mu_i}{\rho_i}\nabla^2 \boldsymbol{u}_i, \tag{2.2a}$$

$$\boldsymbol{\nabla} \cdot \boldsymbol{u}_i = 0, \tag{2.2b}$$

where all quantities are non-dimensional and the Ekman number characterizing the relative importance of viscosity to rotation is defined by $Ek = \mu_0/\rho_0 \Omega a^2$. The non-dimensional density $\rho_i \in [0, 2]$ and the non-dimensional viscosity $\mu_i \in [0, 2]$. We now proceed by defining the linear differential operator, $\mathcal{L}$, by

$$\mathcal{L}[\phi] = \left(\frac{1}{2}\frac{\partial}{\partial t} - \frac{Ek}{2}\frac{\mu_i}{\rho_i}\nabla^2\right)\phi. \tag{2.3}$$

We are able to write the velocity and pressure perturbations to the hydrostatic initial condition in terms of a generalised potential, ϕ, in each layer (Hart 1981) as

$$\boldsymbol{u}_i = \epsilon\left\{\left(1 + \mathcal{L}^2\right)\boldsymbol{\nabla}\phi_i - \mathcal{L}\left[\hat{\boldsymbol{z}} \times \boldsymbol{\nabla}\phi_i\right] + \hat{\boldsymbol{z}} \times \left(\hat{\boldsymbol{z}} \times \boldsymbol{\nabla}\phi_i\right)\right\}, \tag{2.4a}$$

$$p_i = p_{0i}(\boldsymbol{x}, t) - 2\epsilon\rho_i\left(1 + \mathcal{L}^2\right)\mathcal{L}[\phi_i], \tag{2.4b}$$

where $|\epsilon| \ll 1$. For suitable p_{0i} in each layer, this posed ansatz satisfies the equation of motion (2.2*a*) at leading order and at order ϵ. The incompressibility condition (2.2*b*) leads to the governing equation for the generalised potential. Noting that $\boldsymbol{\nabla} \cdot (\hat{\boldsymbol{z}} \times \boldsymbol{\nabla}\phi_i) \equiv 0$

https://doi.org/10.1017/jfm.2020.842 Published online by Cambridge University Press

and that $\boldsymbol{\nabla}\cdot[\hat{\boldsymbol{z}}\times(\hat{\boldsymbol{z}}\times\boldsymbol{\nabla}\phi_i)]=-\nabla_H^2\phi_i$, where we define the horizontal Laplacian $\nabla_H^2=\partial_{rr}+r^{-1}\partial_r+r^{-2}\partial_{\theta\theta}$, we have that

$$\left(1+\mathcal{L}^2\right)\nabla^2\phi_i-\nabla_H^2\phi_i=0, \tag{2.5}$$

a sixth-order, linear partial differential equation for ϕ_i.

The initial unperturbed location of the interface is taken to be at $r=R$ for $R\in(0,1]$ (see figure 1) and we assume that the position of the perturbed interface between the two fluid layers is given by $\mathscr{S}$ where

$$\mathscr{S}:=r-\left(R+\epsilon\cos\left(\frac{n\pi\,[z-\delta]}{2\delta}\right)\exp(\mathrm{i}\,(m\theta+\omega t))\right)=0, \tag{2.6}$$

for axial (varicose) wavenumber $n\in\mathbb{N}$, azimuthal wavenumber $m\in\mathbb{N}$ and domain aspect ratio $\delta=d/a$, and note that this definition of the interface sets the small quantity ϵ. The precession and growth rate of the instability are determined by the real and imaginary parts of ω, respectively. In particular, if $\mathrm{Im}(\omega)<0$ the perturbation to the interface will grow exponentially in time. We now seek normal mode solutions for ϕ, in each layer, of the form

$$\phi_i(\boldsymbol{x},t)=\hat{\phi}_i(r)\cos\left(\frac{n\pi\,[z-\delta]}{2\delta}\right)\exp(\mathrm{i}\,(m\theta+\omega t)). \tag{2.7}$$

We further note that for modified Bessel functions of the first and second kind we have that for a scalar $k\in\mathbb{C}$,

$$\nabla^2[I_m(kr)]=\left(\frac{m^2}{r^2}+k^2\right)I_m(kr),\quad \nabla^2[K_m(kr)]=\left(\frac{m^2}{r^2}+k^2\right)K_m(kr), \tag{2.8a.b}$$

Hence, taking $\hat{\phi}(r)$ as a linear combination of both $I_m(kr)$ and $K_m(kr)$, (2.5) yields an eigenvalue equation for the generalised potential given by

$$\left\{1+\left[\frac{\mathrm{i}\omega}{2}+\frac{Ek}{2}\frac{\mu_i}{\rho_i}\left(\frac{1}{\delta_n^2}-k^2\right)\right]^2\right\}\left(\frac{1}{\delta_n^2}-k^2\right)+k^2=0, \tag{2.9}$$

where we have set $\delta_n=2\delta/(n\pi)$. This is a cubic equation in k^2 that yields six linearly independent solutions for $\hat{\phi}_i$ in each layer corresponding to the three values of $\sqrt{k^2}$ given by (2.9) and the modified Bessel functions of the first and second kind. (By consideration of the appropriate Wronskians for $z\in\mathbb{C}$ it can be shown that $I_m(-z)$ and $K_m(-z)$ are linearly dependent on $I_m(z)$ and $K_m(z)$ so solutions to (2.9) corresponding to $-\sqrt{k^2}$ may be disregarded without loss of generality.) Denoting the three roots of (2.9) as k_{ij}^2 for $j=1,2,3$ for each layer $i=1,2$ we therefore have, taking $k_{ij}=\sqrt{k_{ij}^2}$,

$$\phi_i(r)=\epsilon\cos\left(\frac{z-\delta}{\delta_n}\right)\exp(\mathrm{i}(m\theta+\omega t))\sum_{j=1}^{3}\left[b_{ij}I_m(k_{ij}r)+c_{ij}K_m(k_{ij}r)\right],\quad \text{for } i=1,2. \tag{2.10}$$

Enforcing the requirement that $|\boldsymbol{u}_j|<\infty$ on $r=0$ gives that $c_{1j}=0$ for all j due to the properties of the modified Bessel function K_m at the origin. Hence we have, in general, six unknown coefficients, b_{ij}, three unknown coefficients, c_{2j}, and an unknown quantity ω to determine by appropriate matching and boundary conditions.

https://doi.org/10.1017/jfm.2020.842 Published online by Cambridge University Press

2.1. *Boundary and matching conditions*

The required boundary and matching conditions are split into two groups, the first group being 'universal' and applying in all cases. The second group of conditions apply only when the fluids under consideration are viscous. In the first universal group of conditions are the no-penetration conditions on the boundaries of the domain, and the kinematic and pressure continuity conditions at the interface (conditions of continuity of normal velocity and normal stress at the boundary between the two fluids). The second group of boundary and matching conditions that apply when the fluids are viscous are referred to as 'viscous conditions' and comprise no-slip conditions and the continuity of tangential velocity and tangential stress at the interface $\mathscr{S}$ defined by (2.6).

The first universal boundary and matching conditions are the no-penetration conditions

$$\hat{\boldsymbol{r}}\cdot\boldsymbol{u}_2(r=1)=0 \quad \text{and} \quad \hat{\boldsymbol{z}}\cdot\boldsymbol{u}_i(z=\pm\delta)=0, \quad \text{for } i=1,2. \tag{2.11a,b}$$

It follows from (2.4*a*) that $w_i=\boldsymbol{u}_i\cdot\hat{\boldsymbol{z}}=(1+\mathcal{L}^2)\partial\phi_i/\partial z$ and so w_i is proportional to $\sin([z-\delta]/\delta_n)$ and hence the second of these conditions, $\hat{\boldsymbol{z}}\cdot\boldsymbol{u}_i(z=\pm\delta)=0$, for $i=1,2$ is automatically satisfied.

The interface is described by (2.6) and the associated kinematic conditions are that

$$\left.\frac{\mathrm{D}}{\mathrm{D}t}\left(r-\left[R+\epsilon\cos\left(\frac{z-\delta}{\delta_n}\right)\exp(\mathrm{i}(m\theta+\omega t))\right]\right)\right|_{\mathscr{S}}=0$$

$$\Rightarrow \quad \hat{\boldsymbol{r}}\cdot\boldsymbol{u}_i(r=R)=\epsilon\mathrm{i}\omega\cos\left(\frac{z-\delta}{\delta_n}\right)\exp(\mathrm{i}(m\theta+\omega t)), \tag{2.12}$$

for $i=1,2$ (taking care with the index i, and the unit imaginary number i). The remaining universal matching condition is given by the normal component of the stress continuity condition at the interface.

Denoting by $\Delta\{\cdot\}$ a jump in a quantity from the outer fluid 2 to the inner fluid 1, the stress continuity condition is that

$$\Delta\left\{\boldsymbol{\sigma}_i\cdot\hat{\boldsymbol{n}}\right\}=\frac{1}{We}\left(\nabla\cdot\hat{\boldsymbol{n}}\right)\hat{\boldsymbol{n}}, \tag{2.13}$$

where $\boldsymbol{\sigma}_i=-p_i\boldsymbol{I}+2\mu_i Ek\,\boldsymbol{e}_i$ is the non-dimensional stress tensor, $\boldsymbol{e}_i$ is the non-dimensional rate of strain tensor, $\hat{\boldsymbol{n}}$ is the unit normal to the interface $\mathscr{S}$ pointing from fluid 1 to fluid 2 and We is a Weber number given by $We=\rho_0\Omega^2a^3/\gamma$ where γ is the coefficient of surface tension (cf. Scase & Hill 2018) (We is related to the inverse of the Hocking parameter).

We first satisfy the hydrostatic stress continuity condition that is given by continuity of the pressure across the unperturbed interface $r=R$. It follows from (2.6) and the definition of $\hat{\boldsymbol{n}}$ that on $\mathscr{S}$,

$$\nabla\cdot\hat{\boldsymbol{n}}\big|_{\mathscr{S}}=\frac{1}{R}+\epsilon\left\{\frac{m^2-1}{R^2}+\frac{1}{\delta_n^2}\right\}\cos\left(\frac{z-\delta}{\delta_n}\right)\exp(\mathrm{i}(m\theta+\omega t)). \tag{2.14}$$

Substituting (2.4*b*) into (2.2*a*) with $\boldsymbol{u}_i=\boldsymbol{0}$ we have that the leading-order pressure satisfies $\nabla p_{0i}=\rho_i r\,\hat{\boldsymbol{r}}$ and so take without loss of generality

$$p_{0i}(\boldsymbol{x},t)=\begin{cases}\dfrac{\rho_1}{2}\left(r^2-R^2\right)+\dfrac{1}{We\,R}, & i=1\\[2ex] \dfrac{\rho_2}{2}\left(r^2-R^2\right), & i=2.\end{cases} \tag{2.15}$$

https://doi.org/10.1017/jfm.2020.842 Published online by Cambridge University Press

It follows that on the perturbed interface

$$p_{0i}\big|_{\mathscr{S}} \sim p_{0i}(R) + \epsilon\rho_i R\cos\left(\frac{z-\delta}{\delta_n}\right)\exp(\mathrm{i}(m\theta+\omega t)) + O(\epsilon^2), \tag{2.16}$$

and hence the pressure at the perturbed interface is given by

$$p_i\big|_{\mathscr{S}} \sim p_{0i}(R) + \epsilon\rho_i\left\{R\cos\left(\frac{z-\delta}{\delta_n}\right)\exp(\mathrm{i}(m\theta+\omega t)) - 2\left(1+\mathcal{L}^2\right)\mathcal{L}[\phi_i]\right\} + O(\epsilon^2). \tag{2.17}$$

The continuity of stress $\boldsymbol{\sigma}_i$ across the interface $\mathscr{S}$ in the radial, azimuthal and axial directions is hence given, respectively, by

$$\left[-\epsilon\rho_i\left\{R\cos\left(\frac{z-\delta}{\delta_n}\right)\exp(\mathrm{i}(m\theta+\omega t)) - 2\left(1+\mathcal{L}^2\right)\mathcal{L}[\phi_i]\right\} + 2Ek\,\mu_i\frac{\partial u_i}{\partial r}\right]_-^+$$
$$= \frac{\epsilon}{We}\left(\frac{m^2-1}{R^2}+\frac{1}{\delta_n^2}\right)\cos\left(\frac{z-\delta}{\delta_n}\right)\exp(\mathrm{i}(m\theta+\omega t)), \tag{2.18}$$

$$\left[\mu_i\left(r\frac{\partial}{\partial r}\left(\frac{v_i}{r}\right)+\frac{1}{r}\frac{\partial u_i}{\partial\theta}\right)\right]_-^+ = 0, \tag{2.19a}$$

$$\left[\mu_i\left(\frac{\partial u_i}{\partial z}+\frac{\partial w_i}{\partial r}\right)\right]_-^+ = 0, \tag{2.19b}$$

where $[\,]_-^+$ indicates the jump takes place across the unperturbed interface location, $r=R$ and (2.15) has been used to simplify (2.19).

The condition (2.18) must be satisfied in all cases including the inviscid case when $Ek\equiv 0$, $\mu_i\equiv 0$, and so (2.18) is the final universal boundary and matching condition that is used in conjunction with (2.11) and (2.12). The conditions of tangential stress continuity (2.19) are in the second group of viscous matching conditions that are required when the fluids are viscous.

In the viscous case we must also enforce continuity of tangential velocity at the interface

$$\left[\hat{\boldsymbol{\theta}}\cdot\boldsymbol{u}_i\right]_-^+ = 0, \quad \left[\hat{\boldsymbol{z}}\cdot\boldsymbol{u}_i\right]_-^+ = 0 \tag{2.20a,b}$$

and the no-slip conditions

$$\hat{\boldsymbol{\theta}}\cdot\boldsymbol{u}_2(r=1) = 0, \quad \hat{\boldsymbol{z}}\cdot\boldsymbol{u}_2(r=1) = 0. \tag{2.21a,b}$$

The viscous boundary and matching conditions are given by (2.19), (2.20*a*,*b*) and (2.21*a*,*b*).

2.2. *Inviscid solution*

We first consider solutions to the system in the inviscid case. If the fluids in both layers are inviscid then $Ek=0$. As a result of this assumption, (2.9) becomes linear in k^2 and independent of both μ_i and ρ_i, giving one value of $\sqrt{k^2}$, the same value for each layer. Hence, the number of eigensolutions reduces from nine in the general viscous case to three

https://doi.org/10.1017/jfm.2020.842 Published online by Cambridge University Press

in the present inviscid case. The number of boundary and matching conditions are reduced accordingly since we do not enforce the viscous conditions, i.e. the no-slip conditions or continuity of tangential stress and velocity at the interface.

In the inviscid case (2.9) is reduced to

$$\left(1-\frac{\omega_0^2}{4}\right)\left(\frac{1}{\delta_n^2}-k_0^2\right)+k_0^2=0, \tag{2.22}$$

where we write $k=k_0$ for the unique inviscid wavenumber and $\omega=\omega_0$ for the inviscid eigenvalue, such that the growth rate of an inviscid system is determined by $-\mathrm{Im}(\omega_0)$. As (2.9) in this case is independent of both μ_i and ρ_i, and therefore k is the same in each layer, we take

$$k_i=k_0=\frac{1}{\delta_n}\left(1-\frac{4}{\omega_0^2}\right)^{1/2}, \quad \text{for } i=1,2 \tag{2.23}$$

and the eigensolution in each layer is given by $\phi_i(\boldsymbol{x},t)=\epsilon\hat{\phi}_i(r)\cos([z-\delta]/\delta_n)\exp\{\mathrm{i}(m\theta+\omega_0 t)\}$ where

$$\hat{\phi}_1(r)=b_1 I_m(k_0 r), \quad \hat{\phi}_2(r)=b_2 I_m(k_0 r)+c_2 K_m(k_0 r). \tag{2.24a,b}$$

Substitution into the kinematic condition (2.12) forces

$$\omega_0 R\hat{\phi}_i'(R)+2m\hat{\phi}(R)=-4\mathrm{i}R, \quad i=1,2. \tag{2.25}$$

We define

$$f_I(r)=(\omega_0+2)\,mI_m(r)+\omega_0 rI_{m+1}(r), \tag{2.26a}$$

$$f_K(r)=(\omega_0+2)\,mK_m(r)-\omega_0 rK_{m+1}(r), \tag{2.26b}$$

such that the kinematic condition in the inner and outer layer may be, respectively, expressed as

$$b_1 f_I(k_0R)=-4\mathrm{i}R, \qquad b_2 f_I(k_0R)+c_2 f_K(k_0R)=-4\mathrm{i}R. \tag{2.27a,b}$$

The no-penetration condition on $r=1$ (2.11) requires that

$$b_2 f_I(k_0)+c_2 f_K(k_0)=0. \tag{2.28}$$

Combining (2.24), (2.27) and (2.28) we have that

$$\hat{\phi}_1(r)=-4\mathrm{i}R\frac{I_m(k_0r)}{f_I(k_0R)}, \quad \hat{\phi}_2(r)=4\mathrm{i}R\frac{f_K(k_0)I_m(k_0r)-f_I(k_0)K_m(k_0r)}{f_I(k_0)f_K(k_0R)-f_I(k_0R)f_K(k_0)}. \tag{2.29a}$$

Defining the Atwood number to be

$$\mathscr{A}=\frac{\rho_2-\rho_1}{\rho_2+\rho_1}, \tag{2.30}$$

the pressure continuity condition, (2.18) with $Ek=0$, yields the dispersion relation

$$\left[\frac{1+\mathscr{A}}{\mathscr{A}}\hat{\phi}_2(R)-\frac{1-\mathscr{A}}{\mathscr{A}}\hat{\phi}_1(R)\right]\left(\frac{\omega_0^2}{4}-1\right)\omega_0=2\mathrm{i}R+\frac{\mathrm{i}}{\mathscr{A}We}\left(\frac{m^2-1}{R^2}+\frac{1}{\delta_n^2}\right). \tag{2.31}$$

Note that our definition of the Atwood number, $\mathscr{A}$, is negative for an unstable configuration. This is consistent with, for example, Scase *et al.* (2017*b*) and

https://doi.org/10.1017/jfm.2020.842 Published online by Cambridge University Press

Scase & Hill (2018), but differs in sign from the standard definition used by authors who are considering only an unstable arrangement.

This dispersion relation is consistent with the global stability criteria determined by Joseph *et al.* (1985) (stability when $J > 1$ in their notation; see also Weidman *et al.* (1997)). In the limit $n \to 0$ the two-dimensional dispersion relation (Scase & Hill 2018, (3.16)) is recovered. This follows from $k \sim O(n)$ and small argument approximations to the Bessel function following Abramowitz & Stegun (1964, §§ 9.1.7, 9.1.9) that gives

$$\hat{\phi}_1(R) \sim -\frac{4\mathrm{i}R}{m(\omega_0+2)} + O(n^2), \quad \hat{\phi}_2(R) \sim \frac{4\mathrm{i}\left[R\omega_0\left(1+R^{2m}\right)+2R\left(1-R^{2m}\right)\right]}{m\left(\omega_0^2-4\right)\left(1-R^{2m}\right)} + O(n^2). \tag{2.32a,b}$$

We may also show that for weakly unstable configurations where $-\mathscr{A} \ll 1$ and $\mathscr{A}We = O(1)$, the growth of the unstable modes satisfy

$$\omega_0 \sim \frac{\mathscr{A}\mathrm{i}}{2}\left(\frac{R}{\delta_n}+\frac{m^2\delta_n}{R}\right)\left[1+\frac{1}{2R\mathscr{A}We}\left(\frac{m^2-1}{R^2}+\frac{1}{\delta_n^2}\right)\right] + O(\mathscr{A}^2). \tag{2.33}$$

We now consider the moderating effects of small quantities of fluid viscosity on the inviscid growth rate.

2.3. *Low viscosity solutions*

For fluids with low but non-zero viscosity, $0 < Ek \ll 1$, the growth of the instability behaves as $\omega \sim \omega_0 + \omega_1 Ek^{1/2} + O(Ek)$ where ω_0 is the inviscid solution as described in § 2.2 and ω_1 is the coefficient of the first-order correction. In the limit $Ek \to 0$ the governing wavenumber (2.9) is a singular perturbation problem. The three required roots are the regular inviscid solution and two singular roots. The regular root in each layer $i = 1, 2$ is given by

$$k_{i1} \sim k_0 + \frac{\omega_1}{\omega_0}\left(\frac{1}{\delta_n^2 k_0} - k_0\right) Ek^{1/2} + O\left(Ek\right), \tag{2.34}$$

where k_0 is as defined in (2.23). The two singular roots behave as

$$k_{ij} \sim \mathrm{e}^{\mathrm{i}\pi/4}\left(\frac{\rho_i}{\mu_i}\right)^{1/2}\omega_0^{1/2}Ek^{-1/2}\left\{1+\left[\frac{\omega_1}{2\omega_0} \mp \frac{\mathrm{e}^{\mathrm{i}\pi/4}}{\delta_n}\left(\frac{\mu_i}{\rho_i}\right)^{1/2}\omega_0^{-3/2}\right]Ek^{1/2} + O\left(Ek\right)\right\}, \tag{2.35}$$

for $i = 1, 2$, $j = 2, 3$, where we take $j = 2$ to correspond to choosing the negative sign in (2.35) and $j = 3$ to correspond to choosing the positive sign. We define the viscosity contrast, η, similarly to the Atwood number (2.30) such that

$$\eta = \frac{\mu_2 - \mu_1}{\mu_2 + \mu_1}. \tag{2.36}$$

Now, noting that

$$\frac{\rho_1}{\mu_1} = \frac{1-\mathscr{A}}{1-\eta}, \quad \frac{\rho_2}{\mu_2} = \frac{1+\mathscr{A}}{1+\eta}, \tag{2.37a,b}$$

https://doi.org/10.1017/jfm.2020.842 Published online by Cambridge University Press

ω_0	$1.15 \times 10^{-1} - 2.25\mathrm{i}$	ω_1	$-5.47 \times 10^{-1} + 2.15 \times 10^{1}\mathrm{i}$
k_0	$2.52 \times 10^{1} - 5.64 \times 10^{-1}\mathrm{i}$	—	—
b_{110}	$1.75 \times 10^{-8} + 3.83 \times 10^{-9}\mathrm{i}$	$\hat{b}_{12}$	$-6.75 \times 10^{-2} - 4.08 \times 10^{-2}\mathrm{i}$
b_{210}	$-4.94 \times 10^{-15} - 3.57 \times 10^{-15}\mathrm{i}$	$\hat{b}_{13}$	$-9.17 \times 10^{3} + 5.02 \times 10^{3}\mathrm{i}$
c_{210}	$-9.07 \times 10^{6} + 2.83 \times 10^{6}\mathrm{i}$	$\hat{b}_{22}$	$2.02 \times 10^{-6} + 2.12 \times 10^{-6}\mathrm{i}$
b_{111}	$-1.04 \times 10^{-6} - 1.08 \times 10^{-7}\mathrm{i}$	$\hat{b}_{23}$	$4.82 \times 10^{1} - 1.79 \times 10^{1}\mathrm{i}$
b_{211}	$2.86 \times 10^{-13} + 1.33 \times 10^{-13}\mathrm{i}$	$\hat{c}_{22}$	$8.91 \times 10^{-1} - 4.87 \times 10^{-1}\mathrm{i}$
c_{211}	$-1.00 \times 10^{9} + 4.01 \times 10^{8}\mathrm{i}$	$\hat{c}_{23}$	$6.56 \times 10^{-6} + 3.97 \times 10^{-6}\mathrm{i}$

TABLE 1. Numerical evaluation of the coefficients of the low viscosity expansions in the case $\mathscr{A} = -1/2$, $R = 1/\sqrt{2}$, $m = 3$, $\delta_n = (6\pi)^{-1}$, $\eta = 0$.

the regular behaviour and singular behaviour of the wavenumbers means that we rescale the coefficients of the eigensolutions $I_m(kr)$ and $K_m(kr)$ as

$$b_{11}I_m(kr) = I_m(k_{11}r)\left\{b_{110} + b_{111}Ek^{1/2} + O(Ek)\right\}, \tag{2.38}$$

$$b_{1j}I_m(kr) = \frac{I_m(k_{1j}r)}{I_m\left(\mathrm{e}^{\mathrm{i}\pi/4}R\left[\dfrac{1-\mathscr{A}}{1-\eta}\right]^{1/2}\omega_0^{1/2}Ek^{-1/2}\right)}\left\{\hat{b}_{1j} + O(Ek^{1/2})\right\}, \tag{2.39}$$

for $j = 2, 3$ in the inner layer (defining the constants b_{110}, b_{111} and $\hat{b}_{1j}$) and

$$b_{21}I_m(kr) = I_m(k_{21}r)\left\{b_{210} + b_{211}Ek^{1/2} + O(Ek)\right\}, \tag{2.40}$$

$$b_{2j}I_m(kr) = \frac{I_m(k_{2j}r)}{I_m\left(\mathrm{e}^{\mathrm{i}\pi/4}\left[\dfrac{1+\mathscr{A}}{1+\eta}\right]^{1/2}\omega_0^{1/2}Ek^{-1/2}\right)}\left\{\hat{b}_{2j} + O(Ek^{1/2})\right\}, \tag{2.41}$$

$$c_{21}K_m(kr) = K_m(k_{21}r)\left\{c_{210} + c_{211}Ek^{1/2} + O(Ek)\right\}, \tag{2.42}$$

$$c_{2j}K_m(kr) = \frac{K_m(k_{2j}r)}{K_m\left(\mathrm{e}^{\mathrm{i}\pi/4}R\left[\dfrac{1+\mathscr{A}}{1+\eta}\right]^{1/2}\omega_0^{1/2}Ek^{-1/2}\right)}\left\{\hat{c}_{2j} + O(Ek^{1/2})\right\}, \tag{2.43}$$

in the outer layer, for $j = 2, 3$ (defining the constants b_{210}, b_{211}, c_{210}, c_{211}, $\hat{b}_{2j}$ and $\hat{c}_{2j}$).

The inviscid solution for ω_0 and the associated coefficients b_{110}, b_{210} and c_{210} are given by (2.27), (2.28) and (2.31) and follow from enforcing the universal boundary conditions. The six modified coefficients $\hat{b}_{ij}$ and $\hat{c}_{2j}$ for $i = 1, 2$ and $j = 2, 3$ are determined in terms of the inviscid solution and the corrections b_{111}, b_{211}, c_{211} and ω_1 by enforcing the viscous boundary conditions at first order. These solutions (given in appendix A) may then be substituted into the $O(Ek^{1/2})$ universal conditions yielding a system in the remaining four unknowns, b_{111}, b_{211} c_{211} and ω_1 from which the correction ω_1 may be determined. A particular solution for $\mathscr{A} = -1/2$, $R = 1/\sqrt{2}$, $m = 3$, $\delta_n = (6\pi)^{-1}$, $\eta = 0$ is given in table 1.

https://doi.org/10.1017/jfm.2020.842 Published online by Cambridge University Press

Numerical

k_{11}	$18.85 + 7.29 \times 10^{-4}\mathrm{i}$	b_{11}	$-7.19 \times 10^{-13} + 1.14 \times 10^{-15}\mathrm{i}$	c_{21}	$4.17 \times 10^{-2} + 4.06 \times 10^{-5}\mathrm{i}$
k_{12}	$18.85 - 7.29 \times 10^{-4}\mathrm{i}$	b_{12}	$-7.17 \times 10^{-13} + 2.99 \times 10^{-16}\mathrm{i}$	c_{22}	$4.18 \times 10^{-2} + 2.17 \times 10^{-5}\mathrm{i}$
k_{13}	$18.85 + 1.48 \times 10^{-19}\mathrm{i}$	b_{13}	$-7.17 \times 10^{-13} - 1.44 \times 10^{-15}\mathrm{i}$	c_{23}	$4.18 \times 10^{-2} - 6.24 \times 10^{-5}\mathrm{i}$
k_{21}	$18.85 + 3.51 \times 10^{-4}\mathrm{i}$	b_{21}	$1.13 \times 10^{-16} - 1.00 \times 10^{-19}\mathrm{i}$	ω	$5.56 \times 10^{-14} - 9.10 \times 10^{-7}\mathrm{i}$
k_{22}	$18.85 - 3.51 \times 10^{-4}\mathrm{i}$	b_{22}	$1.13 \times 10^{-16} - 1.51 \times 10^{-20}\mathrm{i}$	—	—
k_{23}	$18.85 + 4.92 \times 10^{-20}\mathrm{i}$	b_{23}	$1.13 \times 10^{-13} + 1.15 \times 10^{-19}\mathrm{i}$	—	—

Asymptotic

k_{11}	$18.85 + 7.29 \times 10^{-4}\mathrm{i}$	α_{11}	-7.18×10^{-9}	α_{22}	4.18×10^{2}
k_{12}	$18.85 - 7.29 \times 10^{-4}\mathrm{i}$	β_{11}	$-2.69 \times 10^{-10} - 1.55 \times 10^{-10}\mathrm{i}$	β_{22}	$-1.16 \times 10^{1} - 6.72 \times 10^{0}\mathrm{i}$
k_{13}	18.85	γ_{11}	$1.13 \times 10^{-9} - 1.96 \times 10^{-9}\mathrm{i}$	γ_{22}	$2.53 \times 10^{1} - 4.39 \times 10^{1}\mathrm{i}$
k_{21}	$18.85 + 3.51 \times 10^{-4}\mathrm{i}$	α_{21}	1.13×10^{-12}	ω_∞	$-9.10 \times 10^{-3}\mathrm{i}$
k_{22}	$18.85 - 3.51 \times 10^{-4}\mathrm{i}$	β_{21}	$2.15 \times 10^{-14} + 1.24 \times 10^{-14}\mathrm{i}$	—	—
k_{23}	18.85	γ_{21}	$-1.14 \times 10^{-13} + 1.97 \times 10^{-13}\mathrm{i}$	—	—

TABLE 2. Numerical and asymptotic approximations in the high viscosity regime for the unknown coefficients and growth rates for parameters $Ek = 10^4$, $\mathscr{A} = -1/2$, $R = 1/\sqrt{2}$, $\delta_n = (6\pi)^{-1}$, $m = 3$, $\eta = 0$. The difference in order of magnitude of coefficients requires a high degree of numerical accuracy to be used. The agreement between the numerical value of ω and the asymptotic value $\omega_\infty\, Ek^{-1}$ is good.

In order to calculate the growth rate correction ω_1 we use the results of (A 1) to write four linear equations for b_{111}, b_{211}, c_{211} and ω_1. We define the functions

$$\hat{f}_I(r) = m\delta_n^2 k_0\omega_0 I_m(k_0 r) + r(\omega_0 - 2)I_{m+1}(k_0 r), \tag{2.44a}$$

$$\hat{f}_K(r) = m\delta_n^2 k_0\omega_0 K_m(k_0 r) - r(\omega_0 - 2)K_{m+1}(k_0 r). \tag{2.44b}$$

Hence we are able to show

$$\begin{aligned}\hat{f}_I(R)b_{111} = &-\frac{\omega_1}{\omega_0^2(\omega_0^2-4)}\left\{b_{110}\left[2\hat{f}_I(R)\left[\omega_0(\omega_0^2-4)+4m\right]\right.\right.\\
&\left.+\ 2k_0\left[m\delta_n^2(-\omega_0+2m)+2R^2\right](\omega_0-2)\omega_0 I_m(k_0R)\right] + 4\mathrm{i}R\delta_n^2k_0\omega_0^2(\omega_0-2)\Big\}\\
&+\mathrm{e}^{-\mathrm{i}\pi/4}\left\{k_0\omega_0(m^2\delta_n^2+R^2)(\omega_0-2)\left[(b_{110}-b_{210})I_m(k_0R)-c_{210}K_m(k_0R)\right]\right.\\
&\left.+2m\left[\hat{f}_I(R)(b_{110}-b_{210})-\hat{f}_K(R)c_{210}\right]\right\}\\
&\times\left\{\omega_0^{3/2}R\left(\frac{1-\mathscr{A}}{1-\eta}\right)^{1/2}\left[1+\left(\frac{1-\mathscr{A}}{1+\mathscr{A}}\right)^{1/2}\left(\frac{1-\eta}{1+\eta}\right)^{1/2}\right]\right\}^{-1},\end{aligned} \tag{2.45a}$$

$$\begin{aligned}\frac{1-\mathscr{A}}{1+\mathscr{A}}b_{111} - b_{211} - \frac{K_m(k_0R)}{I_m(k_0R)}c_{211} = &\frac{\omega_1}{I_m(k_0R)\omega_0(\omega_0^2-4)}\left\{\left(b_{210}-\frac{1-\mathscr{A}}{1+\mathscr{A}}b_{110}\right)\right.\\
&\times\left(4k_0RI_{m+1}(k_0R)+\left[3\omega_0^2+4(m-1)\right]I_m(k_0R)\right)\\
&\left.+\ c_{210}\left[(3\omega_0^2+4(m-1))K_m(k_0R)-4Rk_0K_{m+1}(k_0R)\right]\right\},\end{aligned} \tag{2.45b}$$

https://doi.org/10.1017/jfm.2020.842 Published online by Cambridge University Press

$$\hat{f}_I(R)b_{211}+\hat{f}_K(R)c_{211}=\frac{\omega_1}{\omega_0^2(\omega_0^2-4)}\Big\{2k_0\omega_0(\omega_0-2)\left[(m\delta_n^2(\omega_0-2m)-2R^2)\right.$$
$$\times(I_m(k_0R)b_{210}+c_{210}K_m(k_0R))-2\mathrm{i}R\delta_n^2\omega_0\Big]$$
$$-\left.(2\hat{f}_I(R)b_{210}+2\hat{f}_K(R)c_{210})(\omega_0(\omega_0^2-4)+4m)\right\}$$
$$-\mathrm{e}^{-\mathrm{i}\pi/4}\left\{k_0\omega_0(m^2\delta_n^2+R^2)(\omega_0-2)\left[c_{210}K_m(k_0R)\right.\right.$$
$$\left.+I_m(k_0R)(b_{210}-b_{110})\right]+2m(\hat{f}_K(R)c_{210}+(b_{210}-b_{110})\hat{f}_I(R))\Big\}$$
$$\times\left\{\omega_0^{3/2}R\left(\frac{1+\mathscr{A}}{1+\eta}\right)^{1/2}\left[1+\left(\frac{1+\mathscr{A}}{1-\mathscr{A}}\right)^{1/2}\left(\frac{1+\eta}{1-\eta}\right)^{1/2}\right]\right\}^{-1}, \tag{2.45c}$$

$$\hat{f}_I(1)b_{211}+\hat{f}_K(1)c_{211}=-\frac{2\omega_1}{\omega_0^2(\omega_0^2-4)}\Big\{k_0\omega_0(\omega_0-2)\left[2-m\delta_n^2(\omega_0-2m)\right]$$
$$\times\left(I_m(k_0)b_{210}+K_m(k_0)c_{210}\right)+\left[\omega_0(\omega_0^2-4)+4m\right](\hat{f}_I(1)b_{210}+\hat{f}_K(1)c_{210})\Big\}$$
$$+\mathrm{e}^{-\mathrm{i}\pi/4}\left\{k_0\omega_0(m^2\delta_n^2+1)(I_m(k_0)b_{210}+K_m(k_0)c_{210})(\omega_0-2)+2m(\hat{f}_I(1)b_{210}+\hat{f}_K(1)c_{210})\right\}$$
$$\times\left\{\omega_0^{3/2}\left(\frac{1+\mathscr{A}}{1+\eta}\right)^{1/2}\right\}^{-1}. \tag{2.45d}$$

For parameters $\mathscr{A}=-1/2$, $R=1/\sqrt{2}$, $m=3$, $\delta_n=(6\pi)^{-1}$, $\eta=0$ values of the inviscid solution and the coefficients for the low viscosity asymptotic correction are quoted in table 1. For the same parameters, figure 2(*a*) is a plot of the difference between the exact eigenvalue ω for non-zero Ek, and the inviscid solution ω_0. Both the real and imaginary parts of $\omega-\omega_0$ behave as $Ek^{1/2}$ as $Ek\to 0$, consistently with the asymptotic description. The upper solid line is $\mathrm{Im}(\omega-\omega_0)$ which is positive as the effect of the fluid viscosity is to inhibit the growth of the perturbation. The lower solid line is $-\mathrm{Re}(\omega-\omega_0)$. The dashed straight lines that coincide with the solid lines as $Ek\to 0$ are the correction $\omega_1 Ek^{1/2}$ calculated as described above by solving the linear system (2.45).

Figure 2(*b*) shows contours of $\mathrm{Im}(\omega_0)$, the growth rate of the inviscid solution, for the same Atwood number and initial interface location as figure 2(*a*). The contours show the behaviour of the inviscid system; the higher the azimuthal wavenumber, m, and the higher the axial wavenumber, n (corresponding to lower values of δ_n), the greater the growth rate in general. Figure 2(*c*) shows contours of the imaginary part of the coefficient ω_1. The change in sign compared with $\mathrm{Im}(\omega_0)$ shows that the viscous correction $\omega_1 Ek^{1/2}$ acts to suppress the growth of the perturbation. Contours are shown for $\eta=0$ (solid) where the viscosity is the same in each layer, $\mu_1=\mu_2$. Also shown are contours of $\eta=-1/4$ (dashed) where the inner layer is more viscous than the outer layer, $\mu_1>\mu_2$, and $\eta=1/4$ (dot-dashed) where the inner layer is less viscous than the outer layer, $\mu_1<\mu_2$. For the chosen parameters the plot shows that for a given Ekman number and Atwood number, having the more viscous fluid in the outer layer is more stable than having the more viscous fluid in the inner layer.

The effects of surface tension may be included in the low viscosity correction by using values of b_{110}, b_{210}, c_{210} and ω_0 from the inviscid solution, including surface tension effects, in (2.45). No further modification of the linear system (2.45) for the remaining coefficients

https://doi.org/10.1017/jfm.2020.842 Published online by Cambridge University Press

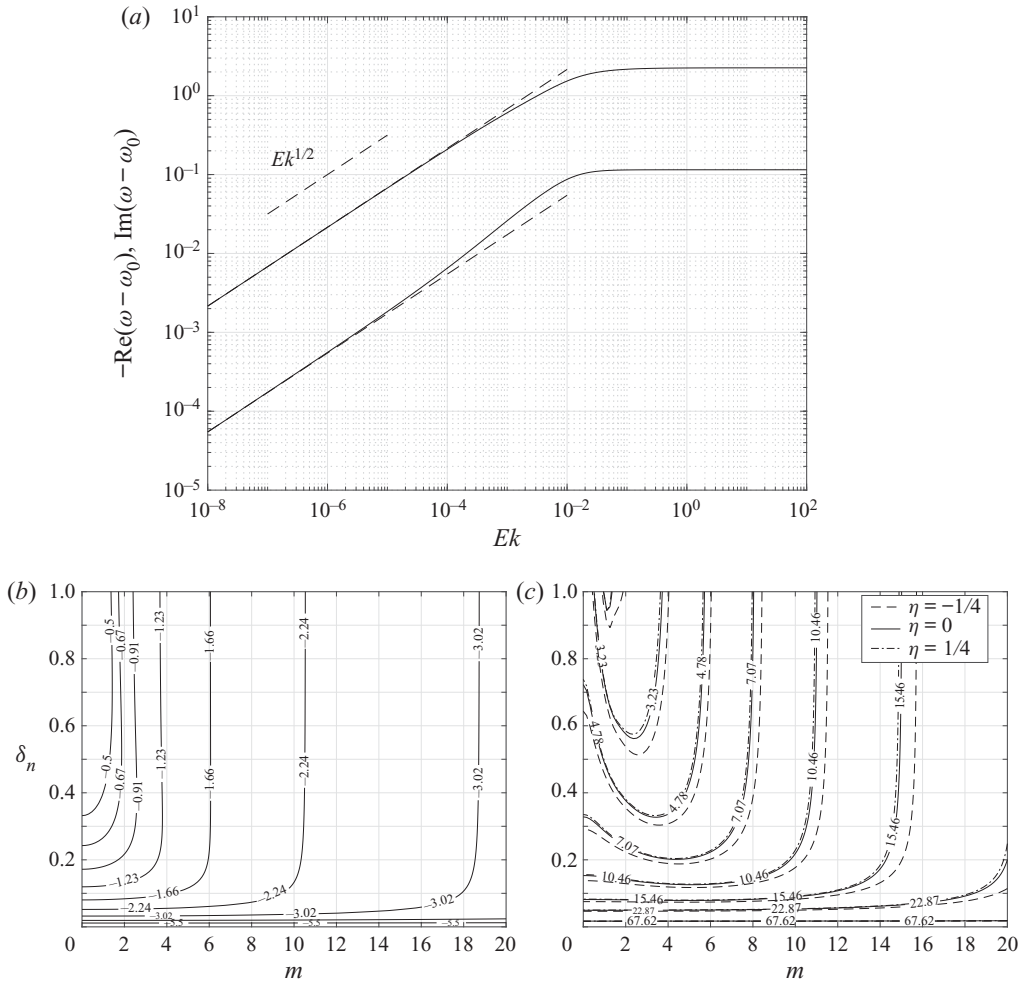


FIGURE 2. (*a*) The solid lines are the real and imaginary parts of the difference between the exact eigenvalue ω calculated numerically and the inviscid eigenvalue ω_0 (the upper line is the imaginary part, the lower line is the real part) for varying Ek. The parameters chosen were $\mathscr{A} = -1/2, R = 1/\sqrt{2}, m = 3, \delta_n = (6\pi)^{-1}$. The imaginary part controls the growth of the instability and the correction to the inviscid growth rate behaves as $Ek^{1/2}$. The dashed lines that coincide with the numerical solution are the asymptotic correction calculated as described in § 2.3. (*b*) Contours of the imaginary part of the inviscid eigenvalue ω_0 for $\mathscr{A} = -1/2, R = 1/\sqrt{2}$. As m and n increase the growth rate of the instability increases. (*c*) Contours of the imaginary part of the order $Ek^{1/2}$ correction, ω_1 for $\mathscr{A} = -1/2, R = 1/\sqrt{2}$. The solid lines are for fluids of equal viscosity $\eta = 0$, the dashed lines are the same value contours, but for an inner layer that is more viscous than the outer with $\eta = -1/4$, and the dot-dashed lines are the same value contours again, but for an outer layer that is more viscous than the inner with $\eta = 1/4$.

b_{111}, b_{211} c_{211} and ω_1 is required. Figure 3 shows an example where $\mathscr{A} = -10^{-2}$, $R = 1/\sqrt{2}, m = 60, \delta_n = (10\pi)^{-1}$, $We = 10^6$, $\eta = 0$. The solution without the correction for surface tension is shown dot-dashed. The asymptotic correction to the inviscid growth rate including the effects of surface tension is shown dashed and behaves as $Ek^{1/2}$, just as

https://doi.org/10.1017/jfm.2020.842 Published online by Cambridge University Press

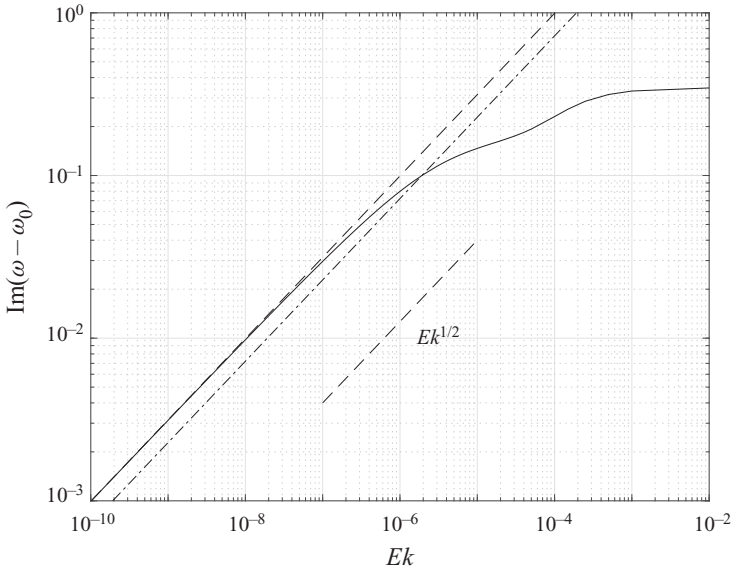


FIGURE 3. The correction to the inviscid solution, ω_0 for $Ek \ll 1$. The chosen parameters were $\mathscr{A} = -10^{-2}$, $R = 1/\sqrt{2}$, $m = 60$, $\delta_n = (10\pi)^{-1}$, $\eta = 0$, $We = 10^6$. The low viscosity asymptotic solution is $\omega \sim 7.58 \times 10^{-3} - 3.47 \times 10^{-1}\mathrm{i} + (-6.70 \times 10^{-1} + 9.94 \times 10^{1}\mathrm{i})Ek^{1/2} + O(Ek)$. The positive imaginary part of the viscous correction shows viscosity damping the growth rate of the mode. The dot-dashed line is the low viscosity behaviour without the correction for surface tension. As the dashed line lies above the dot-dashed line the effect of the surface tension is to further dampen the growth rate of the instability.

the solution without the correction for surface tension. As the surface-tension-corrected solution (dashed) lies above the correction without surface tension (dot-dashed) the effect of the surface tension is to inhibit the growth rate of the instability as might be anticipated on physical grounds.

2.4. *High viscosity solutions*

For very viscous fluids where $Ek \gg 1$ the three solutions for k^2 to the governing wavenumber (2.9) behave as

$$k_{ij}^2 \sim \frac{1}{\delta_n^2} - \lambda_j \left(\frac{2\rho_i}{\delta_n \mu_i}\frac{1}{Ek}\right)^{2/3} + \frac{2\mathrm{i}\rho_i\omega_\infty}{3\mu_i}\frac{1}{Ek^2} + O\left(\frac{1}{Ek^3}\right), \tag{2.46}$$

where $\omega \sim \omega_\infty Ek^{-1} + O(Ek^{-2})$ for the three values $j = 1, 2, 3$ of λ_j that satisfy $\lambda_j^3 = -1$. Specifically we take

$$\lambda_j = \exp\left\{\mathrm{i}\left[2j-3\right]\pi/3\right\} \quad \text{for } j = 1, 2, 3. \tag{2.47}$$

We seek the leading-order growth rate $\omega_\infty Ek^{-1}$ and so must determine the coefficients b_{ij} and c_{2j} for $i = 1, 2$ and $j = 1, 2, 3$ to a high enough order of accuracy that ω_∞ may itself be determined. For each of the nine coefficients, as with (2.46), this requires finding the first three terms of the asymptotic expansion. Motivated by observations from numerical

https://doi.org/10.1017/jfm.2020.842 Published online by Cambridge University Press

solutions we pose, for $i = 1, 2$, that the coefficients be of the form

$$b_{i1} \sim \alpha_{i1}\frac{1}{Ek} + \beta_{i1}\frac{\lambda_1}{Ek^{4/3}} + \gamma_{i1}\frac{\lambda_3}{Ek^{5/3}} + O\left(\frac{1}{Ek^2}\right), \tag{2.48a}$$

$$b_{i2} \sim \alpha_{i1}\frac{1}{Ek} + \beta_{i1}\frac{\lambda_3}{Ek^{4/3}} + \gamma_{i1}\frac{\lambda_1}{Ek^{5/3}} + O\left(\frac{1}{Ek^2}\right), \tag{2.48b}$$

$$b_{i3} \sim \alpha_{i1}\frac{1}{Ek} + \beta_{i1}\frac{\lambda_2}{Ek^{4/3}} + \gamma_{i1}\frac{\lambda_2}{Ek^{5/3}} + O\left(\frac{1}{Ek^2}\right), \tag{2.48c}$$

and similarly for c_{2j} for $j = 1, 2, 3$. This form of approximation to the coefficients replaces the nine unknown general coefficients b_{ij} and c_{2j} with nine unknown coefficients in the large Ek expansion; α_{11} in the inner layer, α_{21} and α_{22} in the outer layer, and similarly for β and γ. The leading and second-order boundary and matching equations at $O(Ek^{-4/3})$ and $O(Ek^{-5/3})$ are automatically satisfied, leaving a system of ten linear equations (see (B 1)–(B 10) in appendix B) in the nine unknown coefficients α, β and γ and the eigenvalue ω_∞ that may be solved by standard methods.

Here we give the solution for ω_∞ in the special case of equal viscosity in each fluid layer, $\eta = 0$ and no surface tension. The general expression for arbitrary η and surface tension is considerably more cumbersome, but may be found from (B 1)–(B 10). We express ω_∞ in terms of the following functions:

$$F_1(r) = 2\delta_n r K_{m+1}\left(\frac{r}{\delta_n}\right) + \left[(m-2)\,m\delta_n^2 + r^2\right] K_m\left(\frac{r}{\delta_n}\right), \tag{2.49a}$$

$$F_2(r) = -\left[(m-2)\frac{m\delta_n^2}{2} + \frac{R^2 r^2}{2}\right] K_{m+1}\left(\frac{1}{\delta_n}\right) + m\delta_n\left[(m-2)m\delta_n^2 + \frac{R^2+r^2}{2}\right] K_m\left(\frac{1}{\delta_n}\right), \tag{2.49b}$$

$$F_3(r) = 2\left(m^2-4\right)m^2\delta_n^4 + \left[m^2(r^2+R^2) + 2m(1+r^2+R^2)\right]\delta_n^2 - R^2\left(1-\frac{r^2}{2}\right). \tag{2.49c}$$

We also define the constants G_1 and G_2 in terms of the parameters m, δ_n and R

$$G_1 = \frac{1}{2}I_{m+1}^3\left(\frac{1}{\delta_n}\right) + \frac{3m+2}{2}\delta_n I_m\left(\frac{1}{\delta_n}\right) I_{m+1}^2\left(\frac{1}{\delta_n}\right) + \left[(m+2)m\delta_n^2 - \frac{1}{2}\right] I_m^2\left(\frac{1}{\delta_n}\right) I_{m+1}\left(\frac{1}{\delta_n}\right) - \frac{m\delta_n}{2} I_m^3\left(\frac{1}{\delta_n}\right), \tag{2.50a}$$

$$G_2 = I_{m+1}\left(\frac{R}{\delta_n}\right) K_m\left(\frac{R}{\delta_n}\right) + K_{m+1}\left(\frac{R}{\delta_n}\right) I_m\left(\frac{R}{\delta_n}\right). \tag{2.50b}$$

https://doi.org/10.1017/jfm.2020.842 Published online by Cambridge University Press

Finally, we define the following five constants in terms of the m, δ_n and R and the functions F_1, F_3 and constants G_1 and G_2:

$$H_1 = \left[(m+2)R^2 - m\right]\delta_n K_{m+1}\left(\frac{1}{\delta_n}\right) + \left[(m-2)m\delta_n^2 + R^2\right]K_m\left(\frac{1}{\delta_n}\right), \tag{2.51a}$$

$$H_2 = \left[(m+2)m\delta_n^2 + R^2\right]RK_{m+1}\left(\frac{R}{\delta_n}\right) - 2m\delta_n F_1(R), \tag{2.51b}$$

$$H_3 = \left[1 + (m+2)^2\delta_n^2\right]K_{m+1}\left(\frac{1}{\delta_n}\right) + 2\delta_n K_m\left(\frac{1}{\delta_n}\right), \tag{2.51c}$$

$$\begin{aligned} H_4 = {} & -m\delta_n\left[(m-2)m\delta_n^2 + R^2\right]K_{m+1}\left(\frac{1}{\delta_n}\right) \\ & + \frac{1}{2}\left[4(m-2)m^3\delta_n^4 + (4R^2+1)m^2\delta_n^2 + R^4\right]K_m\left(\frac{1}{\delta_n}\right), \end{aligned} \tag{2.51d}$$

$$\begin{aligned} H_5 = {} & \frac{R^2}{2}\left\{\left[1 + (m+2)m\delta_n^2\right]K_{m+1}\left(\frac{1}{\delta_n}\right) + (m+2)\delta_n F_1(1)\right\}I_{m+1}^2\left(\frac{R}{\delta_n}\right) \\ & + R\left\{F_3(0)K_m\left(\frac{1}{\delta_n}\right) - \delta_n\left[(m^2-4)m\delta_n^2 + 2R^2(m+1) - m\right]K_{m+1}\left(\frac{1}{\delta_n}\right)\right\} \\ & \times I_m\left(\frac{R}{\delta_n}\right)I_{m+1}\left(\frac{R}{\delta_n}\right) \\ & + \left\{\frac{1}{2}\left(\left[(m+2)m\delta_n^2 - R^2\right](1-R^2) - F_3(0)\right)K_{m+1}\left(\frac{1}{\delta_n}\right)\right. \\ & \left. + m\delta_n\left[F_3(R) - \frac{m\delta_n^2}{2}(m+2)\right]K_m\left(\frac{1}{\delta_n}\right)\right\}I_m^2\left(\frac{R}{\delta_n}\right). \end{aligned} \tag{2.51e}$$

We may now write the coefficient of the asymptotic growth rate as

$$\begin{aligned} \omega_\infty = {} & \frac{\mathrm{i}\mathscr{A}}{RG_1G_2}\left\{\left[m\delta_n I_m^2\left(\frac{1}{\delta_n}\right)F_2(R) - H_4 I_{m+1}^2\left(\frac{1}{\delta_n}\right)\right]I_m^2\left(\frac{R}{\delta_n}\right)\right. \\ & + R\left[\left(m\delta_n H_1 I_m\left(\frac{1}{\delta_n}\right)^2 - 2F_2(1)I_{m+1}^2\left(\frac{1}{\delta_n}\right)\right)I_m\left(\frac{R}{\delta_n}\right) + G_1F_1(R)\right]I_{m+1}\left(\frac{R}{\delta_n}\right) \\ & - \frac{R^2}{2}\left[m\delta_n H_3 I_m^2\left(\frac{1}{\delta_n}\right) + F_1(1)I_{m+1}^2\left(\frac{1}{\delta_n}\right)\right]I_{m+1}\left(\frac{R}{\delta_n}\right)^2 \\ & \left. - G_1H_2I_m\left(\frac{R}{\delta_n}\right) - H_5 I_{m+1}\left(\frac{1}{\delta_n}\right)I_m\left(\frac{1}{\delta_n}\right)\right\}. \end{aligned} \tag{2.52}$$

As with the special $\eta = 0$ case above, for arbitrary η the leading-order growth rate in the absence of surface tension, $\omega_\infty Ek^{-1}$, is linear in the Atwood number, $\mathscr{A}$, and its dependence upon the aspect ratio δ and the axial wavenumber n is only through δ_n. A solution for the purposes of verification of any implementation is provided in table 2.

Figure 4(*a*) shows the behaviour of ω (solid curves) for parameters $\mathscr{A} = -1/2$, $R = 1/\sqrt{2}$, $m = 3$, $\delta_n = (6\pi)^{-1}$, $\eta = 0$ and no surface tension. As $Ek \to \infty$, the imaginary part

https://doi.org/10.1017/jfm.2020.842 Published online by Cambridge University Press

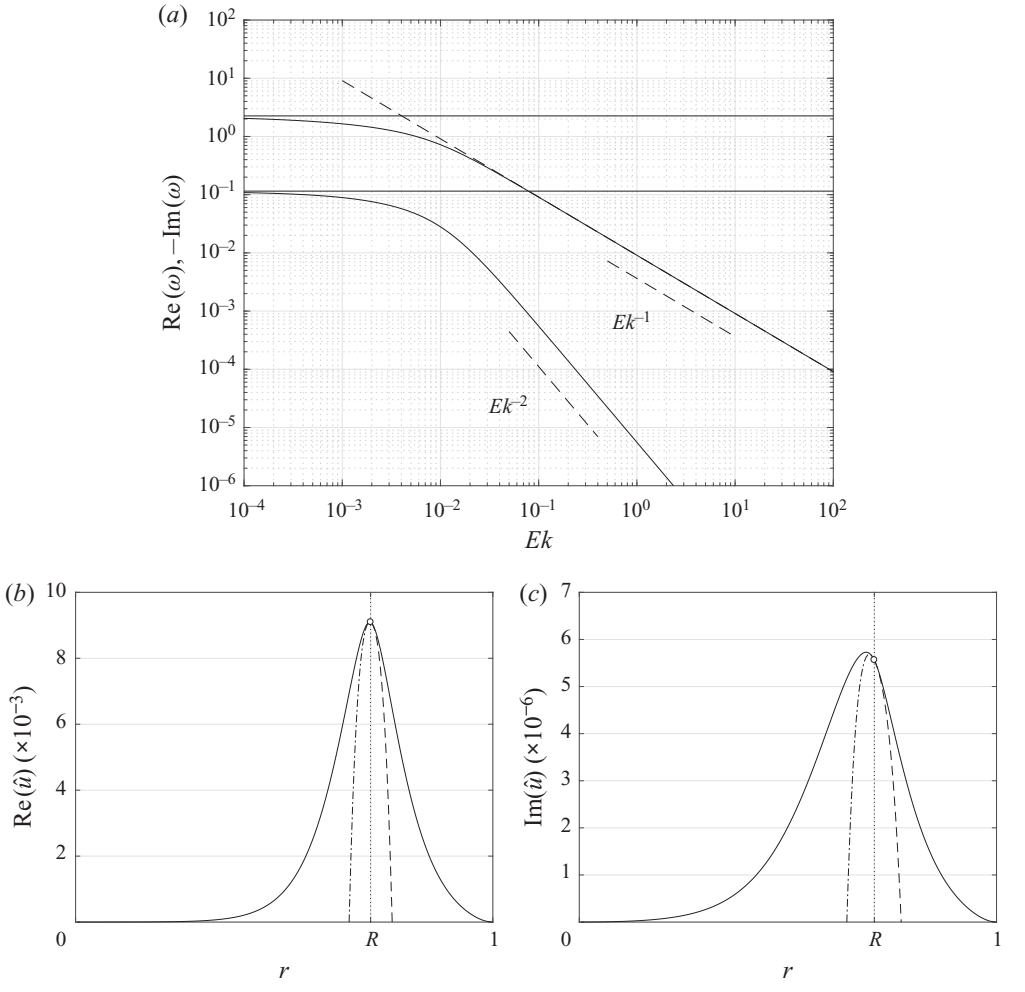


FIGURE 4. Numerical solutions for $\mathscr{A} = -1/2$, $R = 1/\sqrt{2}$, $\eta = 0$, $m = 3$, $\delta_n = (6\pi)^{-1}$. (*a*) The real and (negative) imaginary parts of the eigenvalue ω. The imaginary part controls the growth of the instability and behaves as Ek^{-1} as $Ek \to \infty$. The dashed line that coincides with the numerical solution is calculated using (2.52). The upper horizontal solid line is the imaginary part of the inviscid solution given by (2.31). The real part of the solution behaves as Ek^{-2} as $Ek \to \infty$ and again tends to the real part of the inviscid solution shown by the lower solid horizontal line as $Ek \to 0$. (*b*) The real part of $\hat{u}$ and (c) the imaginary part of $\hat{u}$ where the horizontal velocity is written as $u = \hat{u}(r)\cos(\delta_n^{-1}[z - \delta])\exp(\mathrm{i}(m\theta + \omega t))$ and here $Ek = 1$. The transitions between the inner and outer solutions occur at $r = R$ (vertical dotted line) and are indicated by the white circles.

of ω behaves as Ek^{-1}, whereas the real part behaves as Ek^{-2}. The precession, controlled by $\mathrm{Re}(\omega)$, is suppressed more rapidly than the growth of the perturbation as the Ekman number is increased. The horizontal solid lines are the imaginary (upper) and real (lower) parts of the inviscid solution ω_0. It can be seen that as $Ek \to 0$ the solid curves tend toward the inviscid solution since $\omega \to \omega_0$. The dashed line that coincides with the upper solid curve as $Ek \to \infty$ is the asymptotic high viscosity approximation $-\mathrm{Im}(\omega_\infty Ek^{-1})$ given

https://doi.org/10.1017/jfm.2020.842 Published online by Cambridge University Press

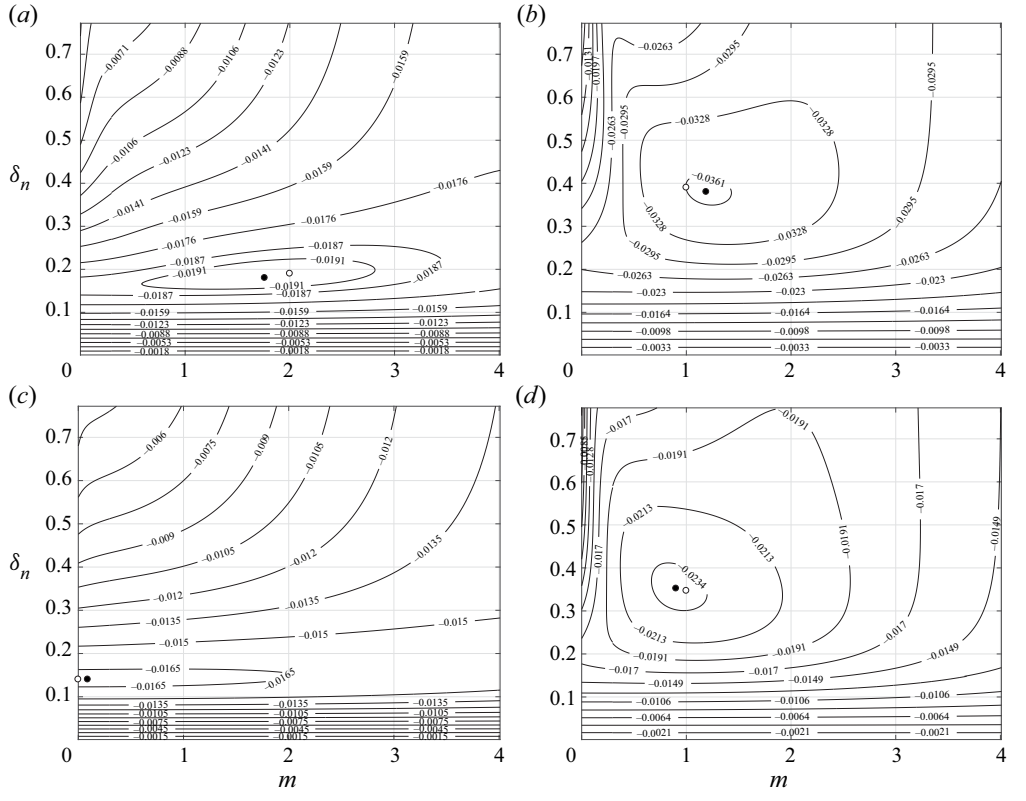


FIGURE 5. Contours of Im(ω), the most unstable mode in the absence of surface tension for: (*a*) $\eta = 0, R = 1/\sqrt{2}$; (*b*) $\eta = -9/11, R = 1/\sqrt{2}$; (*c*) $\eta = 9/11, R = 1/\sqrt{2}$; (*d*) $\eta = 0, R = 1/2$ as a function of azimuthal wavenumber, m, and δ_n. The minimum value in each case is shown by a black circle. The minimum value with m constrained to integer values is shown by a white circle.

by (2.52). This approximation is an estimate of the instability in the high viscosity limit and can be seen to be in good agreement with the numerical value as $Ek \to \infty$.

Figures 4(*b*) and 4(*c*) show typical profiles of the radial dependence of the radial velocity field. Writing $u = \hat{u}(r)\cos(\delta_n^{-1}[z-\delta])\exp(\mathrm{i}(m\theta + \omega t))$ the real and imaginary parts of $\hat{u}$ are shown in figures 4(*b*) and 4(*c*), respectively. The inner layer solutions extend from $r = 0$ to $r = R$ and are shown as solid lines. At $r = R$ the inner solution matches smoothly onto the outer solution as a result of the requirements of continuity of velocity and stress at the interface. The points at which the two solutions match, at $r = R$, is indicated by a white circle. The outer solution extends from $r = R$ to $r = 1$ and is also shown as a solid line. The continuation of the inner layer solution into the outer layer is shown dashed and the continuation of the outer layer solution into the inner layer is shown dot-dashed.

In the absence of surface tension, ω_∞ is proportional to $\mathscr{A}$ and hence the most unstable mode pairing (m, n) is a function of R, δ and η alone. Furthermore, the dependence of ω_∞ on δ and n is through δ_n only. Hence, provided we are in the high viscosity regime, $Ek \gg 1$, and surface tension is negligible, we have that the most unstable mode pairing (m, n), for a given aspect ratio δ is determined by the interface location, R, and the viscosity contrast η alone. Figure 5 shows contours of Im(ω_∞) for different choices of R and η. The minimum value of Im(ω_∞) in each case is shown with a black circle (treating ω_∞ as continuous

https://doi.org/10.1017/jfm.2020.842 Published online by Cambridge University Press

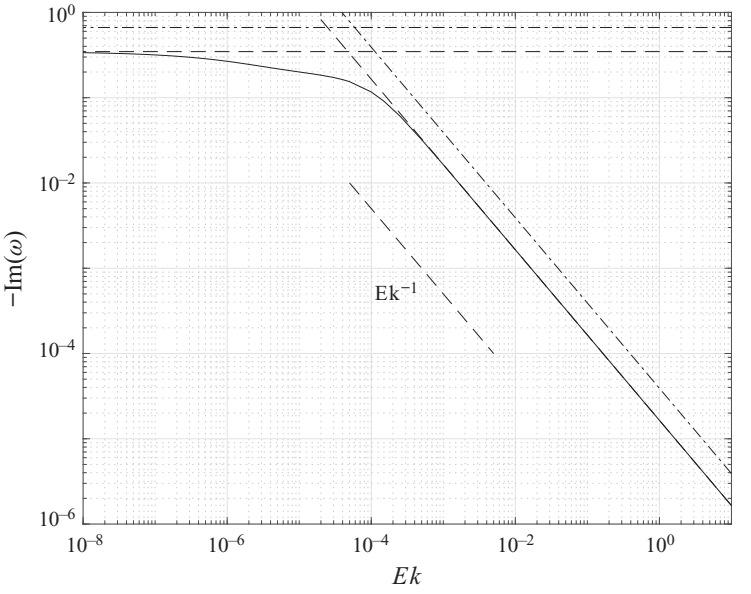


FIGURE 6. The growth rate $-\mathrm{Im}(\omega)$ for the chosen parameters $\mathscr{A} = -10^{-2}$, $R = 1/\sqrt{2}$, $m = 60$, $\delta_n = (10\pi)^{-1}$, $\eta = 0$, $We = 10^6$ (the same parameters as in figure 3). The high-viscosity asymptotic solution is $\omega \sim -1.65 \times 10^{-5}\mathrm{i}Ek^{-1} + O(Ek^{-2})$ shown as the diagonal dashed line. The horizontal dashed and dot-dashed lines are the inviscid solution with and without the correction for surface tension, respectively. The dot-dashed diagonal line is the high viscosity asymptotic solution without the correction for surface tension. As the dot-dashed line lies above the dashed line, as with the low-viscosity case, the effect of the surface tension is to dampen the growth rate of the instability.

in m) and the most unstable mode of growth is shown with a white circle (treating ω_∞ as dependent on $m \in \mathbb{N}$).

In figure 5(a) the parameters are $R = 1/\sqrt{2}$ (equal volumes of fluid in each layer) and $\eta = 0$ (no viscosity contrast between the two layers, $\mu_1 = \mu_2$). Treating ω_∞ as continuous in m, the minimum value of $\mathrm{Im}(\omega_\infty)$ is located at $m = 1.76$, $\delta_n = 0.18$. However, for the most unstable mode of growth we require $m \in \mathbb{N}$ and the minimum subject to this constraint is located at $m = 2$, $\delta_n = 0.19$, an elliptical deformation of the inner fluid layer about the axis.

In figures 5(b) and 5(c) the location of the interface is kept as in figure 5(a), but the viscosity contrast between the layers is varied. In figure 5(b) $\eta = -9/11$ meaning that the inner layer is a factor of 10 times more viscous than the outer layer. The minimum of $\mathrm{Im}(\omega_\infty)$ is located at $m = 1.19$, $\delta_n = 0.38$ and constraining m to integer values gives the most unstable mode at $m = 1$, $\delta_n = 0.39$. This corresponds to a translational motion of the inner layer away from the axis toward the outer boundary.

In figure 5(c) $\eta = 9/11$ meaning that the outer layer is a factor of 10 times more viscous than the inner layer. The minimum of $\mathrm{Im}(\omega_\infty)$ is located at $m = 0.09$, $\delta_n = 0.14$ and corresponds to a most unstable mode given by $m = 0$, $\delta_n = 0.14$. This indicates that the instability develops as a varicose instability, the outer layer is sufficiently viscous that it does not allow the inner layer to move its centre of mass radially and the two fluids tend to change places initially through the growth of axial perturbations alone. The value of $\min\{\mathrm{Im}(\omega)\}$ in figure 5(c) is greater than the value of $\min\{\mathrm{Im}(\omega)\}$ in figure 5(b) indicating

https://doi.org/10.1017/jfm.2020.842 Published online by Cambridge University Press

that, as in the low viscosity limit, for a given Ekman number and Atwood number having the more viscous fluid in the outer layer is more stable than having the more viscous fluid in the inner layer.

Figure 5(*d*) shows contours of $\mathrm{Im}(\omega_\infty)$ for layers of equal viscosity ($\eta = 0$) but with the interface at $R = 1/2$. As with figure 5(*b*), a preference is shown for a translational motion of the inner layer to the outer boundary as the two fluids start to move.

Figure 6 is a comparison of the high viscosity solution with and without surface tension. The solution without the correction for surface tension is shown dot-dashed. The high viscosity asymptotic solution for the growth rate including the effects of surface tension is shown dashed and behaves as Ek^{-1} (just as the solution without the correction for surface tension). As the surface tension solution (dashed) lies below the solution without surface tension (dot-dashed) the effect of the surface tension is as in the low-viscosity case, to inhibit the growth rate of the instability.

3. Numerical simulation of instability

The numerical simulations of the instability were performed using the volume-of-fluid method implemented in the 'interFoam' solver which is part of the OpenFOAM distribution (Weller *et al.* 1998). The solver is reviewed and discussed in Deshpande, Anumolu & Trujillo (2012) and the modifications for use in rotating frames of reference are described in Scase & Hill (2018). A volume-of-fluid approach is used to solve the continuity equation

$$\frac{\partial \rho}{\partial t} + \boldsymbol{\nabla} \cdot (\rho \boldsymbol{u}) = 0 \tag{3.1}$$

and the rotating momentum equation

$$\frac{\partial}{\partial t}(\rho \boldsymbol{u}) + \boldsymbol{\nabla} \cdot (\rho \boldsymbol{u}\boldsymbol{u}) = -\boldsymbol{\nabla} p - \rho \boldsymbol{\Omega} \times (\boldsymbol{\Omega} \times \boldsymbol{x}) - 2\rho \boldsymbol{\Omega} \times \boldsymbol{u} + [\boldsymbol{\nabla} \cdot (\mu \nabla \boldsymbol{u}) + \boldsymbol{\nabla} \boldsymbol{u} \cdot \boldsymbol{\nabla} \mu]\,. \tag{3.2}$$

The solution domain is taken to be a wedge where $r \in [0, 1]$, $\theta \in [-2\pi/m, 2\pi/m]$ and $z \in [-1/2, 1/2]$. For the simulations shown the domain is split into approximately $250 \times 25 \times 250$ cells. The total number of control volumes was greater than 1.5×10^6 and the temporal step size was $\Delta t = 2.5 \times 10^{-3}$. The interface is initially perturbed with an azimuthal wavenumber $m = 60$ and an axial wavenumber $n = 10$. The initial condition in the numerical simulations is that the flow starts from rest in the rotating frame.

Two series of simulations were run, one series in the low viscosity regime and one series in the high viscosity regime. The flow domain had a dimensional radius and height of 10 cm giving an aspect ratio $\delta = 1/2$, the initial unperturbed position of the interface was taken to be $R = 1/\sqrt{2}$ such that the volume of each phase was equal. In the low viscosity regime the two fluid phases had properties similar to those of water with a reference density of 10^3 kg m^{-3} and both layers a dynamic viscosity of 10^{-3} kg m^{-1} s^{-1}. The Atwood number was chosen to be an unstable $\mathscr{A} = -10^{-2}$, and the rotation rate was set at 8π rad s^{-1} or 240 r.p.m. The theoretical predictions are that the non-dimensional inviscid growth rate is given by $-\mathrm{Im}(\omega_0) = 0.67$, the exact growth rate in the low viscosity regime is $-\mathrm{Im}(\omega) = 0.54$, and the low viscosity asymptotics give a predicted growth rate described by $-\mathrm{Im}(\omega_0 + \omega_1 Ek^{1/2}) = 0.52$.

Figure 7 shows the developing interface, defined to be the surface where $\rho = \rho_0$, between the two fluid phases at non-dimensional times $t = 0$, 1.38, 2.14, 2.51 and 3.64 from left to right, respectively, for fluids in the low viscosity regime. The $r = 0$ axis is to

https://doi.org/10.1017/jfm.2020.842 Published online by Cambridge University Press

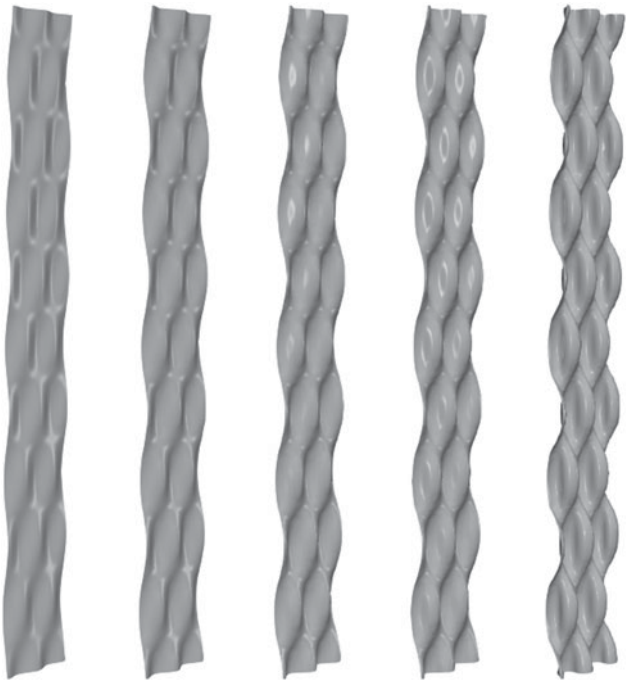


FIGURE 7. The developing instability at the interface for fluids in the low viscosity regime. The simulation parameters were $\mathscr{A} = -0.01$, $R = 1/\sqrt{2}$, $\delta_n = (10\pi)^{-1}$, $m = 60$, $\eta = 0$, $Ek = 3.98 \times 10^{-6}$. The Ekman number follows from a dimensional rotation rate of the system of 8π rad s^{-1} for two fluids with mean dynamic viscosity $\mu_0 = 10^{-3}$ kg m^{-1} s^{-1} and mean density $\rho_0 = 10^3$ kg m^{-3} in a domain of radial extent $a = 0.1$ m. The non-dimensional times shown are $t = 0$, 1.38, 2.14, 2.51 and 3.64 from left to right.

the left of the shown contour as drawn. For $t \gtrsim 2.5$, nonlinear effects start to be observed at the interface.

In the high viscosity regime the two fluid phases had properties similar to those of a dense and viscous black treacle or molasses. The reference fluid density was 1.5×10^3 kg m^{-3} and the dynamic viscosity in each layer was taken as 10 kg m^{-1} s^{-1}, the Atwood number was unchanged at $\mathscr{A} = -10^{-2}$. The rotation rate was 2π rad s^{-1} or 60 r.p.m. The exact theoretical growth rate in the high viscosity regime is given by $-\mathrm{Im}(\omega) = 3.68 \times 10^{-4}$ and the high viscosity asymptotics predict $-\mathrm{Im}(\omega_\infty Ek^{-1}) = 3.68 \times 10^{-4}$.

The simulated and predicted growth rates of the perturbation to the interface in the low viscosity regime are compared in figure 8(*a*). The amplitude of the simulated perturbation to the interface is shown by the circular and square data points, the circular data points are the amplitude of the axial perturbations and the square data points are the amplitude of the azimuthal perturbations. The dashed line is the predicted amplitude using the inviscid model of § 2.2 that gives $\omega_0 = 0.01 - 0.67\mathrm{i}$ for the chosen parameters $\mathscr{A} = -10^{-2}$, $\delta_n = (10\pi)^{-1}$, $m = 60$, $R = 1/\sqrt{2}$. As anticipated on physical grounds, due to the absence of viscosity, the inviscid model overpredicts the growth rate of the perturbation. The dashed-dot line is the asymptotic correction to the inviscid prediction using the low-viscosity solution in § 2.3. With the chosen parameters the simulated Ekman number is $Ek = 3.98 \times 10^{-6}$ and the low-viscosity prediction using § 2.3 is $\omega \sim 0.01 - 0.52\mathrm{i}$. The exact eigenvalue calculated numerically is $\omega = 0.01 - 0.54\mathrm{i}$, and this solution is shown as

https://doi.org/10.1017/jfm.2020.842 Published online by Cambridge University Press

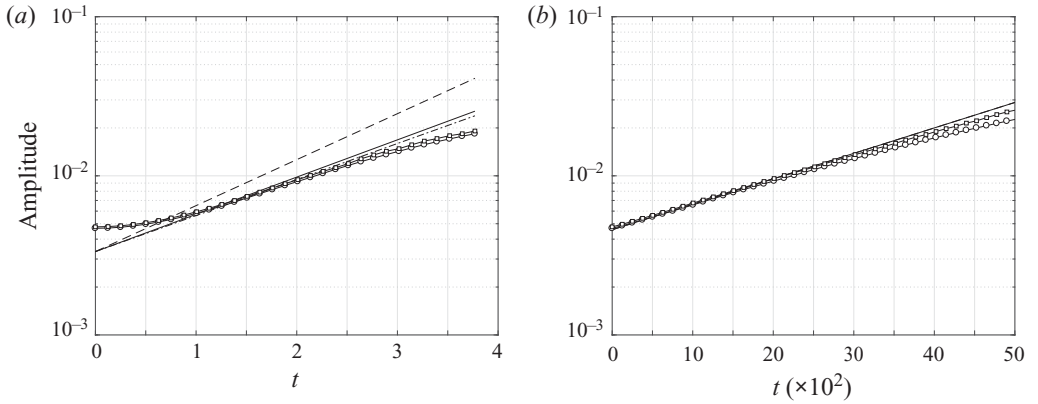


FIGURE 8. The amplitude of the interfacial perturbation with non-dimensional time for parameters $\mathscr{A} = -10^{-2}$, $\delta_n = (10\pi)^{-1}$, $m = 60$, $\eta = 0$. The data points are from the numerical simulation where the amplitude of the perturbation has been calculated by considering the axial perturbation through a meridional plane (circular data points) and the azimuthal perturbation through a horizontal plane (square data points). (*a*) The low viscosity regime: the dashed line is the predicted amplitude from the inviscid model $\omega_0 = 0.01 - 0.67\mathrm{i}$, the dot-dashed line is the low Ekman number asymptotic prediction $\omega \sim 0.01 - 0.52\mathrm{i}$ and the solid line is the exact solution from the full model $\omega = 0.01 - 0.54\mathrm{i}$. (*b*) The high viscosity regime: the solid line is the exact solution calculated from the model $\omega = 9.61 \times 10^{-9} - 3.68 \times 10^{-4}\mathrm{i}$, the dashed line is the amplitude predicted by the high viscosity asymptotics (2.52), $\omega_\infty Ek^{-1} = -3.68 \times 10^{-4}\mathrm{i}$, but cannot be distinguished from the exact solution at the scale shown.

the solid line. As is observed, once the instability starts to grow its growth rate during the linear phase is well-predicted by both the exact solution and the low-viscosity asymptotic model.

Figure 8(*b*) compares the predicted and observed amplitudes of the interfacial perturbation in a high viscosity regime. The circular and square data points indicate the amplitude of the axial and azimuthal perturbations, respectively, as in figure 8(*a*). The solid line follows the exact numerical growth rate $-\mathrm{Im}(\omega) = 3.68 \times 10^4$. Also plotted is a dashed line following the high viscosity asymptotic prediction $-\mathrm{Im}(\omega_\infty Ek^{-1})$, but at the scale shown this lies on top of the exact numerical solution. A good agreement is observed between the predicted growth rate and the observed amplitude of the simulated perturbation.

4. Rotating viscous column

A special case of the configuration of fluids that has been considered so far is that of the rotating viscous liquid column. This situation occurs in the absence of an outer fluid layer, in the limit $\rho_2 \to 0$, $\mu_2 \to 0$. We refer to this limit as the 'viscous column' limit which may be equivalently taken as $\mathscr{A} \to -1$, $\eta \to -1$. The behaviour of liquid columns has received considerable attention in the past, building from the initial work of Rayleigh (1879, 1892) to the inclusion of rotation (Hocking & Michael 1959) and viscosity (Hocking 1960). More recently a linear stability analysis of a uniformly rotating viscous liquid column in the absence of gravity was considered by Kubitschek & Weidman (2007*a*) together with a companion experimental study (Kubitschek & Weidman (2007*b*), where gravity was present) following on from the inviscid studies of Weidman *et al.* (1997) and

https://doi.org/10.1017/jfm.2020.842 Published online by Cambridge University Press

Weidman (1994). In Kubitschek & Weidman (2007*a*) the authors investigated an analytical description of the linear stability of a uniformly rotating viscous column numerically, including showing how their results tend to the established inviscid results in the limit $Ek \to 0$. The authors investigated the preferred mode of instability of a uniformly rotating viscous column as a function of the Ekman number, Ek, and the Weber number, We (Reynolds number, Re, and Hocking parameter, L, in their notation). Through an extensive, careful numerical investigation they were able to establish which mode of instability had the greatest growth rate for a given value of Ek and We and conjectured an asymptotic form of the boundary between the two most unstable modes (an axisymmetric mode and a spiral mode) in the limit of high viscosity and high surface tension (see figure 13 Kubitschek & Weidman (2007*a*), figure 1 Kubitschek & Weidman (2007*b*): the boundary is denoted T_{01}).

Here we are able to compare our general asymptotic approximations derived in § 2 with the special case of a single uniformly rotating viscous column layer. By modifying the dependence of the axial wavenumber and Weber number, such that they depend on the Ekman number, we are able to confirm the conjectured asymptotic form of the T_{01} boundary identified by Kubitschek & Weidman (2007*a*) and find an expression for the boundary that is in good agreement with their numerical estimate.

The boundary between the preferred modes of instability depends upon the growth rate of the most unstable mode in each regime only. The wavelengths of the associated most unstable modes either side of the boundary may be quite different, as may the precession associated with the mode.

In the case of a single fluid layer, the governing system of equations described in § 2 is reduced. The six coefficients, b_{2j} and c_{2j}, describing the behaviour of the outer layer may all be considered identically zero as the outer layer is not present. The three boundary conditions on $r = 1$ for the outer layer, (2.11*a*) and (2.21), the outer layer's kinematic condition, (2.12) (when $i = 2$), and the two conditions of tangential velocity continuity (2.20) (six equations in total) are removed from the system accordingly. This leaves the kinematic condition for the inner (only) layer, and the three free-stress conditions (subject to surface tension) to determine the three remaining coefficients, b_{1j}, and the eigenvalue ω. Hence the system is reduced from ten equations in ten unknowns to four equations in four unknowns.

Kubitschek & Weidman (2007*a*) considered an infinitely long column of radius a subject to axial, azimuthal and temporal perturbations of the form $\exp\{st + \mathrm{i}(n\theta + kz)\}$, in their notation, subject to rotation, viscosity and surface tension described in terms of a non-dimensional Reynolds number, Re, and non-dimensional Hocking parameter, L. As a result of the choice of domain there is not a unique mapping between their variables and those used in the present study, but a natural choice is to take

$$\mathscr{A} = -1, \quad \eta = -1 \text{ (the viscous column limit)} \quad \text{and} \quad R = 1. \tag{4.1a–c}$$

Then, writing terms in the present notation on the left and terms in the notation of Kubitschek & Weidman (2007*a*) on the right, we have the equivalence

$$Ek \leftrightarrow \frac{1}{Re}, \quad We \leftrightarrow \frac{1}{2L}, \quad m \leftrightarrow n, \quad \delta_n \leftrightarrow \frac{1}{k}, \quad \omega \leftrightarrow -\mathrm{i}s. \tag{4.2a–e}$$

Kubitschek & Weidman (2007*a*) consider the growth rates for axisymmetric ($m = 0$) disturbances of wavelength $\delta_n = 1$ and show that in the limit $Ek \to 0$ the growth rates approach the inviscid growth rate, as may be anticipated (see Kubitschek & Weidman 2007*a*, figure 3). The numerical calculation is repeated here, by way of verification of

https://doi.org/10.1017/jfm.2020.842 Published online by Cambridge University Press

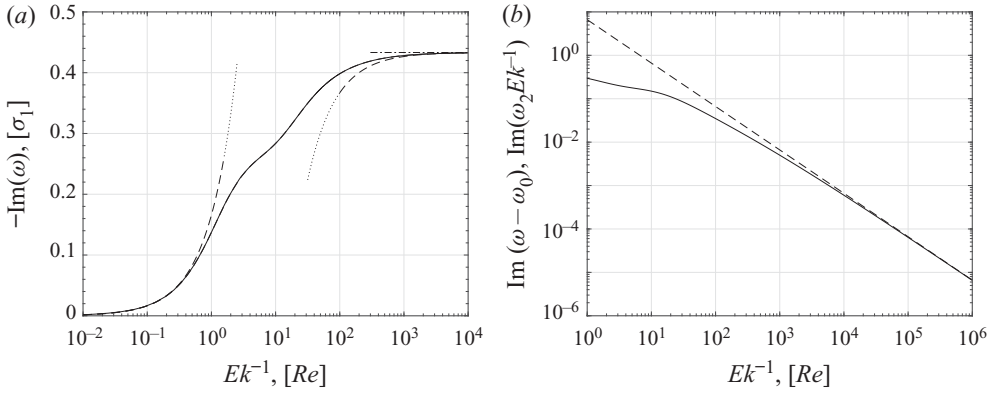


FIGURE 9. (*a*) The numerical solution for the imaginary part of ω in the rotating viscous column reduced system with $\mathscr{A} = -1$, $\eta = -1$, $R = 1$, $m = 0$, $\delta_n = 1$. In this limit the solution is independent of the Weber number, *We*. The solution of Kubitschek & Weidman (2007*a*) figure 3 is shown solid and the present solution is shown dashed, overlaid and the two curves coincide. The inviscid solution due to (2.31) is the horizontal dashed line $\omega_0 \approx -0.433\mathrm{i}$. The high viscosity asymptotic approximation is the dashed curve on the left, given by (4.3). The low viscosity asymptotic approximation is the dashed curve on the right, given by $\omega \approx \omega_0 + \omega_2 Ek$, where ω_2 is given by (4.4). (*b*) A comparison of the imaginary part of $\omega - \omega_0$ (solid) and the imaginary part of $\omega_2 Ek$ (dashed). As the Ekman number increases it can be seen that the imaginary part of $\omega - \omega_0$ tends toward the imaginary part of $\omega_2 Ek$ in agreement with the asymptotic expansion. (Quantities in square brackets use the notation of Kubitschek & Weidman (2007*a*).)

our results, and the imaginary part is shown (dashed) overlaying their solution (solid) in figure 9(*a*). The solutions are seen to coincide. The inviscid solution $-\mathrm{Im}(\omega) = 0.433$ is shown as the horizontal dot-dashed line and is given by solution of (2.31) in the viscous column limit with $R = 1$, $m = 0$ and $\delta_n = 1$. In this special case, the eigenvalue ω is independent of the Weber number, *We*. The asymptotic approximation in the high viscosity limit may be determined from the viscous column approximation to (B 1), (B 3), (B 7) and (B 8) and for $R = 1$, $m = 0$ and $\delta_n = 1$ is given by

$$\omega \sim -\frac{I_1(1)^2\mathrm{i}}{2I_0(1)^2 - 4I_1(1)^2} Ek^{-1} + O(Ek^{-2}) \approx -0.166\mathrm{i}\, Ek^{-1}, \tag{4.3}$$

shown as the dashed curved line on the left-hand side of figure 9(*a*) that tends toward the numerical solutions as $Ek \to \infty$, $Re \to 0$. For general m and δ_n the approximation in the limit $Ek \to \infty$ is given in appendix C (C 1).

The correction to the inviscid growth rate in the low viscosity limit as calculated from § 2.3 is of the form $\omega \sim \omega_0 + \omega_1 Ek^{1/2} + O(Ek)$. However, in the special viscous column limit the coefficient ω_1 is identically zero, and so if a higher-order approximation than the leading-order inviscid approximation is sought, a further term in the expansion is required. Following the same method as in § 2.3 taking the viscous column limit with $R = 1$, the eigenvalue $\omega \sim \omega_0 + \omega_2 Ek + O(Ek^{3/2})$ where ω_0 is the inviscid eigenvalue given by (2.31) and the correction term is given in appendix C (C 2). In the special case considered in

https://doi.org/10.1017/jfm.2020.842 Published online by Cambridge University Press

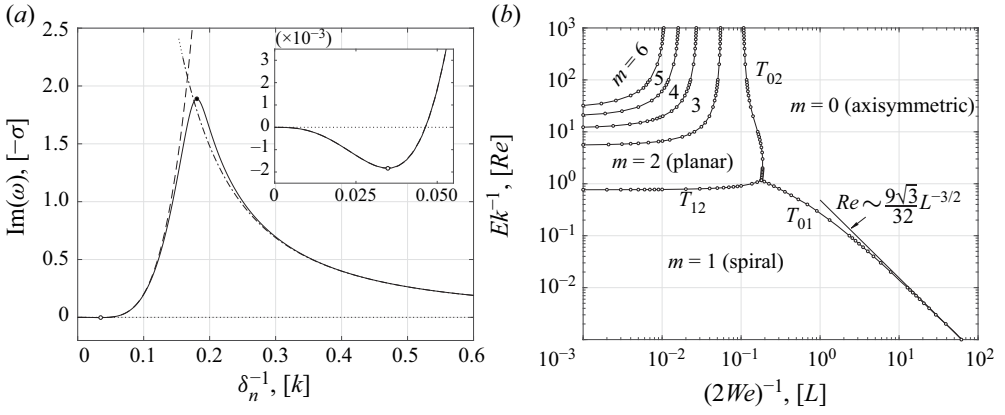


FIGURE 10. (*a*) A numerical solution of the reduced system for $Ek = 10^4$, $We = (10^{-8/3})/2$, $m = 1$. The high viscosity asymptotics of § 2.4, where We and δ_n are fixed, is shown dot-dashed. Scaling the Weber number as $Ek^{-2/3}$ and δ_n as $\delta_n \sim Ek^{1/3}$ leads to the approximation (4.5) which is shown dashed. The estimated most unstable mode is shown as the white data point. An enlargement of the approximation (dashed) in the neighbourhood of this turning point is compared with the numerics (solid) in the inset. The estimated most unstable mode is in good agreement with the full numerical solution. (*b*) The preferred mode diagram of Kubitschek & Weidman (2007*a*, figure 13) is reproduced with the asymptotic approximation to the T_{01} boundary, $Re \sim 9\sqrt{3}/32\, L^{-3/2}$, indicated by the arrow. (Quantities in square brackets use the notation of Kubitschek & Weidman (2007*a*).)

figure 9(*a*) for axisymmetric instability, $m = 0$, and $\delta_n = 1$ there is simplification and

$$\omega_2 = \frac{2\mathrm{i}}{\omega_0^2 k_0}\left\{\left[\omega_0^4 - 8k_0^2 - 16\right] I_1(k_0)^2 - 2k_0\left[\omega_0^4 - 3\omega_0^2 + 4\right] I_0(k_0) I_1(k_0) + 8k_0^2 I_0(k_0)^2\right\}$$
$$\times\left\{k_0\left(4 + [\omega_0^2 k_0]^2\right) I_0(k_0)^2 - \left[\left(4 + \omega_0^2\right) I_0(k_0) + 4k_0 I_1(k_0)\right] I_1(k_0)\right\}^{-1}, \tag{4.4}$$

where k_0 is given by (2.23) and approximately $\omega \sim -0.433\mathrm{i} + 6.63\mathrm{i}\, Ek$. This approximation is shown as the curved dashed line on the right-hand side of figure 9(*a*) that coincides with the numerical solutions as $Ek \to 0$, $Re \to \infty$. The difference between the imaginary part of the full viscous eigenvalue, ω, and the inviscid eigenvalue, ω_0, is shown (solid line) in figure 9(*b*). The first term of the asymptotic approximation to this difference, $\omega_2 Ek$, is shown dot-dashed and is in good agreement as $Ek \to 0$.

Kubitschek & Weidman (2007*a*) focused interest upon which of all the modes of instability has the highest growth rate for a given Ekman number and Weber number, as it might be anticipated that this dominant mode may be the observed mode of instability in a given realisation of the flow. The question of which mode is preferred, and the boundaries between these modes, were presented in their figure 13 (reproduced here in figure 10*b*). They note that in the high viscosity, high surface tension limit the two most unstable modes are the $m = 1$ 'spiral' mode instability and the $m = 0$ axisymmetric mode instability. They further conjecture that the boundary between these two modes appears to follow asymptotic behaviour of the approximate form $Re \sim 0.5 L^{-3/2}$, in their notation.

A solution of the reduced system in this approximate region of parameter space is shown in figure 10(*a*) (solid line) for $Ek = 10^4$, $L = 10^{8/3}$ $(= Ek^{2/3})$, $\alpha = 1$, $m = 1$. The high viscosity asymptotics of § 2.4 for large Ekman number and fixed Weber number and δ_n is shown dot-dashed. The approximation is in good agreement in the region $\delta_n^{-1} \gtrsim 0.3$,

https://doi.org/10.1017/jfm.2020.842 Published online by Cambridge University Press

but does not capture the behaviour of the full numerical solution for $\delta_n^{-1} \lesssim 0.2$. As Ek is increased the turning point of the solution at $\delta_n^{-1} \approx 0.181$, $\mathrm{Im}(\omega) \approx 1.89$ (indicated by the black circle) moves to the left, and the region in which the asymptotic approximation does not agree with the full numerical solution decreases. Indeed, as Ek increases for any fixed δ_n and We the asymptotic approximation improves, as it must. However, the approximation does not capture the behaviour of the most unstable part of the solution if we treat the Weber number and δ_n as fixed parameters rather than coupling the Weber number and δ_n to the Ekman number. In order to capture the behaviour in the region $\delta_n^{-1} \lesssim 0.2$ we require a different asymptotic approximation to ω, where We and δ_n are not fixed, but are proportional to powers of Ek.

In the region of (Re, L) space where $Re \sim L^{-3/2}$ we pose that the most unstable mode solutions to the reduced system in the $m = 1$ spiral mode case behave as $\delta_n \sim Ek^{1/3}$, $We \sim Ek^{-2/3}$, and $\omega \sim \omega_0^* + \omega_1^* Ek^{-1/3} + O(Ek^{-2/3})$, where ω_0^* is real and leads to precession of the mode only, rather than growth. (Equivalently in the notation of Kubitschek & Weidman (2007*a*), $k \sim Ek^{-1/3}$, $L \sim Ek^{2/3}$, which implies $k \sim Re^{1/3}$, $L \sim Re^{-2/3}$.) Here ω_0^* is distinct from the inviscid solution, ω_0, given by (2.31). We seek solutions of the reduced system where $We = \alpha^2 Ek^{-2/3}/2$, $\delta_n = K^{-1} Ek^{1/3}$ where α and K are positive real constants of proportionality. We find in the $m = 1$ spiral mode case that

$$\omega \sim 1 - \frac{K}{\alpha} + \frac{3\mathrm{i}}{8}(K - \alpha) K^3 Ek^{-1/3} + O\left(Ek^{-2/3}\right). \tag{4.5}$$

The growth rate of this spiral mode is $O(Ek^{-1/3})$ and the most unstable mode is given by the stationary point at $K = 3\alpha/4$ where $\omega \sim 1/4 - (3\alpha)^4 \mathrm{i} 2^{-11} Ek^{-1/3}$. The imaginary part of the approximation (4.5) is shown in figure 10(*a*) (dashed) and compares well with the full numerical solution (solid) in the region $\delta_n^{-1} \lesssim 0.2$. The estimate of the location and magnitude of the maximum growth rate given by $\min\{\mathrm{Im}(\omega)\}$ is shown as the white circular data point. The neighbourhood of this turning point is shown enlarged in the inset where again the full numerical solution is shown as the solid line and the asymptotic approximation is shown dashed. The approximation is in excellent agreement with the numerical solution.

The equivalent result for the $m = 0$ axisymmetric mode is

$$\omega \sim -\frac{\mathrm{i}}{6\alpha^2} Ek^{-1/3} + O\left(Ek^{-2/3}\right), \tag{4.6}$$

independent of K. There is no precession of the axisymmetric mode, but the growth rate is $O(Ek^{-1/3})$, the same order of magnitude as the $m = 1$ spiral mode. This therefore confirms the conjectured form of the T_{01} boundary by Kubitschek & Weidman (2007*a*) and we are thus able to determine the value of α at which the preferred mode transitions from $m = 0$ axisymmetric instability to $m = 1$ spiral instability. The two growth rates are equal when

$$\frac{(3\alpha)^4}{2^{11}} = \frac{1}{6\alpha^2}, \tag{4.7}$$

balancing powers of $Ek^{-1/3}$. The only positive real solution to (4.7) is $\alpha = (4/3)^{5/6}$, which gives the T_{01} boundary as $Re \sim 9\sqrt{3}/32\, L^{-3/2} \approx 0.487 L^{-3/2}$ in the notation of Kubitschek & Weidman (2007*a*), in good agreement with their numerical estimate.

The straightforward forms of (4.5) and (4.6) do not reflect the manipulations required to determine them. Asymptotic approximations to the coefficients b_{1j} are required, and these series begin at $O(Ek^{1/3})$ and descend in powers of $Ek^{1/9}$. Sufficient terms to determine

https://doi.org/10.1017/jfm.2020.842 Published online by Cambridge University Press

b_{1j} at $O(Ek^{-5/9})$ are required for the solution to be determined. Similarly the required solution to (2.9) is a series that begins at $O(Ek^{-1/3})$ and also descends in powers of $Ek^{1/9}$ and must be expanded to $O(Ek^{-11/9})$ in order to determine ω_0^* and ω_1^*.

5. Discussion and conclusions

We have investigated the three-dimensional centrifugally driven Rayleigh–Taylor instability, in particular the very high rotational limit of the rotating Rayleigh–Taylor instability in which the effects of gravity may be neglected. A cylindrical domain and initially cylindrical interface between the two fluid layers have been modelled. We have considered the inviscid case, the low viscosity case and the high viscosity case. In all three cases the system is subject to linear instability when the inner layer is denser than the outer layer or, equivalently, the Atwood number, as we have defined it, is negative.

We defined a non-dimensional Ekman number in terms of the mean viscosity, mean density, rotation rate and domain radius such that the low viscosity regime is characterised by a small Ekman number and the high viscosity regime is characterised by a typically large Ekman number. The growth and precession rates in the low viscosity regime are an $O(Ek^{1/2})$ correction to the inviscid growth and precession rate. The growth rate in the high viscosity regime is $O(Ek^{-1})$ while the precession rate is $O(Ek^{-2})$.

In the stable configuration ($\mathscr{A} > 0$) a similar asymptotic dependence on the Ekman number is observed. In the low viscosity limit the oscillation rate and precession rate behave as an $O(Ek^{1/2})$ correction to the inviscid oscillation and precession rate. In the high viscosity limit the oscillation and precession rate behave as $O(Ek^{-1})$.

In the unstable high viscosity limit the growth rate behaves as $O(Ek^{-1})$ and in the special case that surface tension may be neglected has a linear dependence on the Atwood number. This means that the preferred mode of instability in this limit is independent of the absolute values of the viscosity and independent of the density in each layer; the preferred mode in this limit is determined only by the aspect ratio of the domain, δ, the non-dimensional viscosity contrast, η and the initial location of the unperturbed interface, R.

Finally, we showed how our results apply to the special limiting case of a rotating viscous column of fluid in the absence of gravity. For fixed wavenumber and Weber number our asymptotics describe the growth rate of perturbations to the rotating viscous column when the density and viscosity of the outer fluid layer a taken to be zero. In contrast to the general two-layer arrangement, in this special single fluid layer case, in the low viscosity limit, there is an $O(Ek)$ correction to the inviscid growth rate. The boundary over which the preferred mode of growth changes from varicose to spiral in a high viscosity, high surface tension regime is shown to behave as $Ek \sim 2^{7/2}3^{-5/2}We^{-3/2} \approx 0.726We^{-3/2}$.

Our results follow from a linear stability analysis and so are subject to the usual caveats. We cannot draw conclusions relating to any subcritical instability or nonlinear interactions between the various possible modes of instability.

Acknowledgements

The authors would like to acknowledge the financial support of the Woods Hole GFD Summer Program 2018, where this research was initiated. We would also like to thank an anonymous referee for encouraging us to compare our results with those of Kubitschek & Weidman (2007*a*).

https://doi.org/10.1017/jfm.2020.842 Published online by Cambridge University Press

Declaration of interests

The authors report no conflict of interest.

Appendix A. Low viscosity asymptotic system

The coefficients $\hat{b}_{ij}$, $\hat{c}_{2j}$ for $i = 1, 2$, $j = 2, 3$ are shown here for completeness, but their values do not need to be explicitly determined if only the growth rate correction, ω_1, is required;

$$\hat{b}_{12} = -\frac{\mathrm{e}^{\mathrm{i}R/(\omega_0\delta_n)}}{8}\exp\left\{-\mathrm{e}^{\mathrm{i}\pi/4}\frac{\sqrt{1-\mathscr{A}}}{\sqrt{1-\eta}}\frac{R\omega_1}{2\omega_0^{1/2}}\right\}\left\{R\left[1+\left(\frac{1-\mathscr{A}}{1+\mathscr{A}}\right)^{1/2}\left(\frac{1-\eta}{1+\eta}\right)^{1/2}\right]\right\}^{-1}$$
$$\times\left\{-2\mathrm{i}\left[c_{210}K_{m+1}(k_0R)+I_{m+1}(k_0R)\,(b_{110}-b_{210})\right]\delta_n k_0\omega_0 R\right.$$
$$\left.+\left[(\mathrm{i}\delta_n m+R)\,\omega_0-2R\right]\left[(b_{210}-b_{110})I_m(k_0R)+c_{210}K_m(k_0R)\right](\omega_0+2)\right\} \quad (\mathrm{A}\,1a)$$

$$\hat{b}_{13} = \frac{\mathrm{e}^{-\mathrm{i}R/(\omega_0\delta_n)}}{8}\exp\left\{-\mathrm{e}^{\mathrm{i}\pi/4}\frac{\sqrt{1-\mathscr{A}}}{\sqrt{1-\eta}}\frac{R\omega_1}{2\omega_0^{1/2}}\right\}\left\{R\left[1+\left(\frac{1-\mathscr{A}}{1+\mathscr{A}}\right)^{1/2}\left(\frac{1-\eta}{1+\eta}\right)^{1/2}\right]\right\}^{-1}$$
$$\times\left\{-2\mathrm{i}\left[c_{210}K_{m+1}(k_0R)+I_{m+1}(k_0R)\,(b_{110}-b_{210})\right]\delta_n k_0\omega_0 R\right.$$
$$\left.+\left[(\mathrm{i}\delta_n m-R)\,\omega_0+2R\right]\left[(-b_{110}+b_{210})I_m(k_0R)+c_{210}K_m(k_0R)\right](\omega_0+2)\right\} \quad (\mathrm{A}\,1b)$$

$$\hat{b}_{22} = \frac{\mathrm{e}^{\mathrm{i}/(\omega_0\delta_n)}}{8}\exp\left\{-\mathrm{e}^{\mathrm{i}\pi/4}\frac{\sqrt{1+\mathscr{A}}}{\sqrt{1+\eta}}\frac{\omega_1}{2\omega_0^{1/2}}\right\}$$
$$\times\left\{2\mathrm{i}\omega_0 k_0\delta_n\,(b_{210}I_{m+1}(k_0)-c_{210}K_{m+1}(k_0))\right.$$
$$\left.+(\omega_0+2)(\mathrm{i}m\omega_0\delta_n+\omega_0-2)(I_m(k_0)b_{210}+K_m(k_0)c_{210})\right\} \quad (\mathrm{A}\,1c)$$

$$\hat{b}_{23} = -\frac{\mathrm{e}^{-\mathrm{i}/(\omega_0\delta_n)}}{8}\exp\left\{-\mathrm{e}^{\mathrm{i}\pi/4}\frac{\sqrt{1+\mathscr{A}}}{\sqrt{1+\eta}}\frac{\omega_1}{2\omega_0^{1/2}}\right\}$$
$$\times\left\{2\mathrm{i}\omega_0 k_0\delta_n\,(b_{210}I_{m+1}(k_0)-c_{210}K_{m+1}(k_0))\right.$$
$$\left.+(\omega_0+2)(\mathrm{i}m\omega_0\delta_n-\omega_0+2)(I_m(k_0)b_{210}+K_m(k_0)c_{210})\right\} \quad (\mathrm{A}\,1d)$$

$$\hat{c}_{22} = -\frac{\mathrm{e}^{-\mathrm{i}R/(\omega_0\delta_n)}}{8}\exp\left\{\mathrm{e}^{\mathrm{i}\pi/4}\frac{\sqrt{1+\mathscr{A}}}{\sqrt{1+\eta}}\frac{R\omega_1}{2\omega_0^{1/2}}\right\}\left\{R\left[1+\left(\frac{1+\mathscr{A}}{1-\mathscr{A}}\right)^{1/2}\left(\frac{1+\eta}{1-\eta}\right)^{1/2}\right]\right\}^{-1}$$
$$\times\left\{-2\mathrm{i}\left[c_{210}K_{m+1}(k_0R)+I_{m+1}(k_0R)\,(b_{110}-b_{210})\right]\delta_n k_0\omega_0 R\right.$$
$$\left.+\left[(\mathrm{i}\delta_n m-R)\,\omega_0+2R\right]\left[(b_{210}-b_{110})I_m(k_0R)+c_{210}K_m(k_0R)\right](\omega_0+2)\right\} \quad (\mathrm{A}\,1e)$$

$$\hat{c}_{23} = \frac{\mathrm{e}^{\mathrm{i}R/(\omega_0\delta_n)}}{8}\exp\left\{\mathrm{e}^{\mathrm{i}\pi/4}\frac{\sqrt{1+\mathscr{A}}}{\sqrt{1+\eta}}\frac{R\omega_1}{2\omega_0^{1/2}}\right\}\left\{R\left[1+\left(\frac{1+\mathscr{A}}{1-\mathscr{A}}\right)^{1/2}\left(\frac{1+\eta}{1-\eta}\right)^{1/2}\right]\right\}^{-1}$$
$$\times\left\{-2\mathrm{i}\left[c_{210}K_{m+1}(k_0R)+I_{m+1}(k_0R)\,(b_{110}-b_{210})\right]\delta_n k_0\omega_0 R\right.$$
$$\left.+\left[(\mathrm{i}\delta_n m+R)\,\omega_0-2R\right]\left[(b_{210}-b_{110})I_m(k_0R)+c_{210}K_m(k_0R)\right](\omega_0+2).\right\} \quad (\mathrm{A}\,1f)$$

https://doi.org/10.1017/jfm.2020.842 Published online by Cambridge University Press

Appendix B. High viscosity asymptotic system

The universal boundary and matching conditions are given by: the kinematic condition for the inner layer,

$$\left[\left(m^2\delta_n^2+R^2\right)\alpha_{11}-\mathrm{i}m\delta_n^2\left(\frac{2}{\delta_n}\right)^{2/3}\left(\frac{1-\eta}{1-\mathscr{A}}\right)^{1/3}\lambda_2\beta_{11}\right]I_m\left(\frac{R}{\delta_n}\right)$$
$$+\lambda_2\left(\frac{2}{\delta_n}\right)^{1/3}\left(\frac{1-\eta}{1-\mathscr{A}}\right)^{2/3}\left[m\delta_n I_m\left(\frac{R}{\delta_n}\right)+RI_{m+1}\left(\frac{R}{\delta_n}\right)\right]\gamma_{11}=\frac{2\mathrm{i}R\delta_n^2}{3}\omega_0; \quad \text{(B 1)}$$

the kinematic condition for the outer layer,

$$-\mathrm{i}m\lambda_2\delta_n^2\left(\frac{2}{\delta_n}\right)^{2/3}\left(\frac{1+\eta}{1+\mathscr{A}}\right)^{1/3}\left[I_m\left(\frac{R}{\delta_n}\right)\beta_{21}+K_m\left(\frac{R}{\delta_n}\right)\beta_{22}\right]$$
$$+\lambda_2\left(\frac{2}{\delta_n}\right)^{1/3}\left(\frac{1+\eta}{1+\mathscr{A}}\right)^{2/3}\left\{\left[m\delta_n I_m\left(\frac{R}{\delta_n}\right)+RI_{m+1}\left(\frac{R}{\delta_n}\right)\right]\gamma_{21}\right.$$
$$\left.+\left[m\delta_n K_m\left(\frac{R}{\delta_n}\right)-RK_{m+1}\left(\frac{R}{\delta_n}\right)\right]\gamma_{22}\right\}$$
$$+\left[m^2\delta_n^2 I_m\left(\frac{R}{\delta_n}\right)+R^2 I_m\left(\frac{R}{\delta_n}\right)\right]\alpha_{21}+\left[m^2\delta_n^2 K_m\left(\frac{R}{\delta_n}\right)+R^2 K_m\left(\frac{R}{\delta_n}\right)\right]\alpha_{22}$$
$$=\frac{2\mathrm{i}R\delta_n^2}{3}\omega_0; \quad \text{(B 2)}$$

the normal (radial) stress continuity condition,

$$\frac{2}{\delta_n}\left[\left((m-1)m\delta_n^2+R^2\right)m\delta_n I_m\left(\frac{R}{\delta_n}\right)+\left(m^2\delta_n^2+R^2\right)RI_{m+1}\left(\frac{R}{\delta_n}\right)\right]$$
$$\times\left[(1-\eta)\alpha_{11}-(1+\eta)\alpha_{21}\right]-\frac{2}{\delta_n}\left[\left((m-1)m\delta_n^2+R^2\right)m\delta_n K_m\left(\frac{R}{\delta_n}\right)\right.$$
$$\left.-\left(m^2\delta_n^2+R^2\right)RK_{m+1}\left(\frac{R}{\delta_n}\right)\right](1+\eta)\alpha_{22}-\mathrm{i}\lambda_2 m\delta_n^2\left(\frac{2}{\delta_n}\right)^{5/3}$$
$$\times\left\{\left[(m-1)\delta_n I_m\left(\frac{R}{\delta_n}\right)+RI_{m+1}\left(\frac{R}{\delta_n}\right)\right]\left[\frac{(1-\eta)^{4/3}}{(1-\mathscr{A})^{1/3}}\beta_{11}-\frac{(1+\eta)^{4/3}}{(1+\mathscr{A})^{1/3}}\beta_{21}\right]\right.$$
$$\left.-\left[(m-1)\delta_n K_m\left(\frac{R}{\delta_n}\right)-RK_{m+1}\left(\frac{R}{\delta_n}\right)\right]\frac{(1+\eta)^{4/3}}{(1+\mathscr{A})^{1/3}}\beta_{22}\right\}$$
$$+\lambda_2\left(\frac{2}{\delta_n}\right)^{4/3}\left\{\left[\left((m-1)m\delta_n^2+R^2\right)I_m\left(\frac{R}{\delta_n}\right)-R\delta_n I_{m+1}\left(\frac{R}{\delta_n}\right)\right]\right.$$
$$\left.\times\left[\frac{(1-\eta)^{5/3}}{(1-\mathscr{A})^{2/3}}\gamma_{11}-\frac{(1+\eta)^{5/3}}{(1+\mathscr{A})^{2/3}}\gamma_{21}\right]\right.$$

https://doi.org/10.1017/jfm.2020.842 Published online by Cambridge University Press

$$-\left[\left((m-1)m\delta_n^2+R^2\right)K_m\left(\frac{R}{\delta_n}\right)+R\delta_n K_{m+1}\left(\frac{R}{\delta_n}\right)\right]\frac{(1+\eta)^{5/3}}{(1+\mathscr{A})^{2/3}}\gamma_{22}\Bigg\}$$
$$=-\frac{4\delta_n^2R^3\mathscr{A}}{3}-\frac{2}{3\,We}\left[\left(m^2-1\right)\delta_n^2+R^2\right], \tag{B 3}$$

(the final term in the right-hand side of (B 3) is the only surface tension term in the whole system (B 1)–(B 10)); the final universal condition is the no-penetration condition on $r=1$,

$$-\mathrm{i}m\delta_n^2\left(\frac{2}{\delta_n}\right)^{2/3}\left(\frac{1+\eta}{1+\mathscr{A}}\right)^{1/3}\left[I_m\left(\frac{1}{\delta_n}\right)\beta_{21}+K_m\left(\frac{1}{\delta_n}\right)\beta_{22}\right]$$
$$+\lambda_1\left(1+m^2\delta_n^2\right)\left[I_m\left(\frac{1}{\delta_n}\right)\alpha_{21}+K_m\left(\frac{1}{\delta_n}\right)\alpha_{22}\right]+\left(\frac{2}{\delta_n}\right)^{1/3}\left(\frac{1+\eta}{1+\mathscr{A}}\right)^{2/3}$$
$$\times\left\{\left[m\delta_n I_m\left(\frac{1}{\delta_n}\right)+I_{m+1}\left(\frac{1}{\delta_n}\right)\right]\gamma_{21}+\left[m\delta_n K_m\left(\frac{1}{\delta_n}\right)-K_{m+1}\left(\frac{1}{\delta_n}\right)\right]\gamma_{22}\right\}=0. \tag{B 4}$$

The viscous boundary and matching conditions are given by: the azimuthal velocity continuity condition,

$$\left[m\delta_n I_m\left(\frac{R}{\delta_n}\right)+RI_{m+1}\left(\frac{R}{\delta_n}\right)\right]$$
$$\times\left\{\mathrm{i}m\left(\alpha_{11}-\alpha_{21}\right)+\lambda_2\left(\frac{2}{\delta_n}\right)^{2/3}\left[\left(\frac{1-\eta}{1-\mathscr{A}}\right)^{1/3}\beta_{11}-\left(\frac{1+\eta}{1+\mathscr{A}}\right)^{1/3}\beta_{21}\right]\right\}$$
$$-\left[m\delta_n K_m\left(\frac{R}{\delta_n}\right)-RK_{m+1}\left(\frac{R}{\delta_n}\right)\right]\left[\mathrm{i}m\alpha_{22}+\lambda_2\left(\frac{2}{\delta_n}\right)^{2/3}\left(\frac{1+\eta}{1+\mathscr{A}}\right)^{1/3}\beta_{22}\right]$$
$$+\mathrm{i}m\lambda_2\left(\frac{2}{\delta_n}\right)^{1/3}\left\{\left(\frac{1-\eta}{1-\mathscr{A}}\right)^{2/3}I_m\left(\frac{R}{\delta_n}\right)\gamma_{11}\right.$$
$$\left.-\left(\frac{1+\eta}{1+\mathscr{A}}\right)^{2/3}\left[I_m\left(\frac{R}{\delta_n}\right)\gamma_{21}+K_m\left(\frac{R}{\delta_n}\right)\gamma_{22}\right]\right\}=0; \tag{B 5}$$

the axial velocity continuity condition,

$$\left[(m+2)\delta_n I_m\left(\frac{R}{\delta_n}\right)+RI_{m+1}\left(\frac{R}{\delta_n}\right)\right]\left(\alpha_{11}-\alpha_{21}\right)$$
$$-\left[(m+2)\delta_n K_m\left(\frac{R}{\delta_n}\right)-RK_{m+1}\left(\frac{R}{\delta_n}\right)\right]\alpha_{22}+\lambda_2\left(\frac{2}{\delta_n}\right)^{1/3}\left\{\left(\frac{1-\eta}{1-\mathscr{A}}\right)^{2/3}I_m\left(\frac{R}{\delta_n}\right)\gamma_{11}\right.$$
$$\left.-\left(\frac{1+\eta}{1+\mathscr{A}}\right)^{2/3}\left[I_m\left(\frac{R}{\delta_n}\right)\gamma_{21}+K_m\left(\frac{R}{\delta_n}\right)\gamma_{22}\right]\right\}=0; \tag{B 6}$$

https://doi.org/10.1017/jfm.2020.842 Published online by Cambridge University Press

the azimuthal stress continuity condition,

$$\begin{aligned}
&\mathrm{i}m\lambda_1\left\{\left[\left((m-1)m\delta_n^2+R^2\right)I_m\left(\frac{R}{\delta_n}\right)-R\delta_n I_{m+1}\left(\frac{R}{\delta_n}\right)\right][(1+\eta)\alpha_{21}-(1-\eta)\alpha_{11}]\right.\\
&\quad\left.+\left[\left((m-1)m\delta_n^2+R^2\right)K_m\left(\frac{R}{\delta_n}\right)+R\delta_n K_{m+1}\left(\frac{R}{\delta_n}\right)\right](1+\eta)\alpha_{22}\right\}\\
&\quad-\left(\frac{2}{\delta_n}\right)^{2/3}\left\{\left[\left((m-1)m\delta_n^2+\frac{R^2}{2}\right)I_m\left(\frac{R}{\delta_n}\right)\right.\right.\\
&\quad\left.\left.-R\delta_n I_{m+1}\left(\frac{R}{\delta_n}\right)\right]\left[\frac{(1-\eta)^{4/3}}{(1-\mathscr{A})^{1/3}}\beta_{11}-\frac{(1+\eta)^{4/3}}{(1+\mathscr{A})^{1/3}}\beta_{21}\right]\right.\\
&\quad\left.-\left[\left((m-1)m\delta_n^2+\frac{R^2}{2}\right)K_m\left(\frac{R}{\delta_n}\right)+R\delta_n K_{m+1}\left(\frac{R}{\delta_n}\right)\right]\frac{(1+\eta)^{4/3}}{(1+\mathscr{A})^{1/3}}\beta_{22}\right\}\\
&\quad-\mathrm{i}\left(\frac{2}{\delta_n}\right)^{1/3}m\left\{\left[(m-1)\delta_n I_m\left(\frac{R}{\delta_n}\right)+RI_{m+1}\left(\frac{R}{\delta_n}\right)\right]\right.\\
&\quad\times\left[\frac{(1-\eta)^{5/3}}{(1-\mathscr{A})^{2/3}}\gamma_{11}-\frac{(1+\eta)^{5/3}}{(1+\mathscr{A})^{2/3}}\gamma_{21}\right]\\
&\quad\left.-\left[(m-1)\delta_n K_m\left(\frac{R}{\delta_n}\right)-RK_{m+1}\left(\frac{R}{\delta_n}\right)\right]\frac{(1+\eta)^{5/3}}{(1+\mathscr{A})^{2/3}}\gamma_{22}\right\}=0; \qquad \text{(B 7)}
\end{aligned}$$

the axial stress continuity condition,

$$\begin{aligned}
&\frac{2}{\delta_n}\left[\left((m+1)m\delta_n^2+R^2\right)I_m\left(\frac{R}{\delta_n}\right)+R\delta_n I_{m+1}\left(\frac{R}{\delta_n}\right)\right][(1-\eta)\alpha_{11}-(1+\eta)\alpha_{21}]\\
&\quad-\frac{2}{\delta_n}\left[\left((m+1)m\delta_n^2+R^2\right)K_m\left(\frac{R}{\delta_n}\right)-R\delta_n K_{m+1}\left(\frac{R}{\delta_n}\right)\right](1+\eta)\alpha_{22}\\
&\quad-\mathrm{i}\lambda_2\left(\frac{2}{\delta_n}\right)^{2/3}m\delta_n\left\{I_m\left(\frac{R}{\delta_n}\right)\left[\frac{(1-\eta)^{4/3}}{(1-\mathscr{A})^{1/3}}\beta_{11}-\frac{(1+\eta)^{4/3}}{(1+\mathscr{A})^{1/3}}\beta_{21}\right]\right.\\
&\quad\left.-K_m\left(\frac{R}{\delta_n}\right)\frac{(1+\eta)^{4/3}}{(1+\mathscr{A})^{1/3}}\beta_{22}\right\}\\
&\quad+\lambda_2\left(\frac{2}{\delta_n}\right)^{4/3}\left\{\left[m\delta_n I_m\left(\frac{R}{\delta_n}\right)+RI_{m+1}\left(\frac{R}{\delta_n}\right)\right]\left[\frac{(1-\eta)^{5/3}}{(1-\mathscr{A})^{2/3}}\gamma_{11}-\frac{(1+\eta)^{5/3}}{(1+\mathscr{A})^{2/3}}\gamma_{21}\right]\right.\\
&\quad\left.-\left[m\delta_n K_m\left(\frac{R}{\delta_n}\right)-RK_{m+1}\left(\frac{R}{\delta_n}\right)\right]\frac{(1+\eta)^{5/3}}{(1+\mathscr{A})^{2/3}}\gamma_{22}\right\}=0; \qquad \text{(B 8)}
\end{aligned}$$

the azimuthal no-slip condition,

$$\left[m\delta_n I_m\left(\frac{1}{\delta_n}\right)+I_{m+1}\left(\frac{1}{\delta_n}\right)\right]\left[m\lambda_1\alpha_{21}-\mathrm{i}\left(\frac{2}{\delta_n}\right)^{2/3}\left(\frac{1+\eta}{1+\mathscr{A}}\right)^{1/3}\beta_{21}\right]$$

https://doi.org/10.1017/jfm.2020.842 Published online by Cambridge University Press

$$+\left[m\delta_n K_m\left(\frac{1}{\delta_n}\right)-K_{m+1}\left(\frac{1}{\delta_n}\right)\right]\left[m\lambda_1\alpha_{22}-\mathrm{i}\left(\frac{2}{\delta_n}\right)^{2/3}\left(\frac{1+\eta}{1+\mathscr{A}}\right)^{1/3}\beta_{22}\right]$$
$$+m\left(\frac{2}{\delta_n}\right)^{1/3}\left(\frac{1+\eta}{1+\mathscr{A}}\right)^{2/3}\left[I_m\left(\frac{1}{\delta_n}\right)\gamma_{21}+K_m\left(\frac{1}{\delta_n}\right)\gamma_{22}\right]=0; \tag{B 9}$$

and finally the axial no-slip condition,

$$\left[(m+2)\delta_n I_m\left(\frac{1}{\delta_n}\right)+I_{m+1}\left(\frac{1}{\delta_n}\right)\right]\alpha_{21}+\left[(m+2)\delta_n K_m\left(\frac{1}{\delta_n}\right)-K_{m+1}\left(\frac{1}{\delta_n}\right)\right]\alpha_{22}$$
$$+\left(\frac{2}{\delta_n}\right)^{1/3}\left(\frac{1+\eta}{1+\mathscr{A}}\right)^{2/3}\lambda_2\left[K_m\left(\frac{1}{\delta_n}\right)\gamma_{22}+I_m\left(\frac{1}{\delta_n}\right)\gamma_{21}\right]=0. \tag{B 10}$$

Appendix C. Rotating viscous column system

In (4.3) the high viscosity approximation for the rotating viscous column in the axisymmetric case $m=0$, with $\delta_n=1$ was given. It is a special case of the general approximation,

$$\begin{aligned}\omega\sim\frac{\mathrm{i}Ek^{-1}}{4We}&\left\{2\delta_n I_{m+1}^3(\delta_n^{-1})+\left[(m+6)m\delta_n^2-1\right]I_m(\delta_n^{-1})I_{m+1}(\delta_n^{-1})^2\right.\\
&+2\left[(m+2)m\delta_n^2-1\right]m\delta_n I_m^2(\delta_n^{-1})I_{m+1}(\delta_n^{-1})-2m^2\delta_n^2 I_m^3(\delta_n^{-1})\Big\}\\
&\times\left[(m^2-2We-1)\delta_n^2+1\right]\Big\{\Big[1+m(m^3+6m^2-m-6)\delta_n^4\\
&+(2m^2-6m+1)\delta_n^2\Big]I_m(\delta_n^{-1})I_{m+1}^2(\delta_n^{-1})+2\delta_n\left[(m^3+2m^2-m-2)m^2\delta_n^4\right.\\
&+(2m^2-3m+1)m\delta_n^2+m+1\Big]I_m^2(\delta_n^{-1})I_{m+1}(\delta_n^{-1})\\
&+2\delta_n\left[(m^2-1)\delta_n^2-1\right]I_{m+1}^3(\delta_n^{-1})\\
&-\left[1+(m^2+2m-3)m^2\delta_n^4+2(m-1)m\delta_n^2\right]I_m^3(\delta_n^{-1})\Big\}^{-1}.\end{aligned} \tag{C 1}$$

This expression is determined by taking the viscous column approximation, $\mathscr{A}=-1$, $\eta=-1$, to (B 1), (B 3), (B 7) and (B 8), and setting $R=1$.

In (4.4) the low viscosity approximation for the rotating viscous column in the axisymmetric case $m=0$, with $\delta_n=1$ was given. The general approximation for arbitrary m and δ_n is given by

$$\begin{aligned}\omega_2=\frac{2\mathrm{i}}{\delta_n^2\omega_0^2}&\left[(m^2-2We-1)\delta_n^2+1\right]\Big\{(\omega_0^2-4)\left[8+\omega_0^2(4m\omega_0-\omega_0^2-4)\delta_n^2\right]I_{m+1}(k_0)^2\\
&+2\left[m\omega_0^2(\omega_0+2)^2(m-1)\delta_n^2+\omega_0^4-3\omega_0^2+4(2m+1)\right]k_0\delta_n^2\omega_0^2 I_m(k_0)I_{m+1}(k_0)\\
&+2(\omega_0+2)\left[m^2\omega_0^4(\omega_0+2)(m-1)\delta_n^4\right.\\
&+\left.m\omega_0^2(\omega_0+2)(\omega_0-1)^2\delta_n^2-4(\omega_0-2)\right]I_m(k_0)^2\Big\}\\
&\times\Big\{\left[(m^2-2We-1)\delta_n^2+1\right]\left[4k_0 I_{m+1}(k_0)+(\omega_0^2+8m+4)I_m(k_0)\right]k_0\delta_n^2\omega_0^2 I_{m+1}(k_0)\\
&+(\omega_0+2)\left[(\omega_0+2)\left(2\left[(\omega_0-2)^2-m\right]We+m\left(m^2-1\right)\right)\delta_n^4\omega_0^2\right.\\
&+\left.\left[m\omega_0^2(\omega_0+2)-4(m^2-2We-1)(\omega_0-2)\right]\delta_n^2-4(\omega_0-2)\right]I_m(k_0)^2\Big\}^{-1}.\end{aligned} \tag{C 2}$$

https://doi.org/10.1017/jfm.2020.842 Published online by Cambridge University Press

REFERENCES

ABRAMOWITZ, M. & STEGUN, I. A., (Eds) 1964 *Handbook of Mathematical Functions with Formulas, Graphs, and Mathematical Tables*. United States Department of Commerce, National Bureau of Standards.

BALDWIN, K. A., SCASE, M. M. & HILL, R. J. A. 2015 The inhibition of the Rayleigh–Taylor instability by rotation. *Sci. Rep.* **5**, 11706.

BOFFETTA, G. & MAZZINO, A. 2017 Incompressible Rayleigh–Taylor turbulence. *Annu. Rev. Fluid Mech.* **49**, 119–143.

CARNEVALE, G. F., ORLANDI, P., ZHOU, Y. & KLOOSTERZIEL, R. C. 2002 Rotational suppression of Rayleigh–Taylor instability. *J. Fluid Mech.* **457**, 181.

CHANDRASEKHAR, S. 1961 *Hydrodynamic and Hydromagnetic Stability*. Dover.

CHEN, X. M., SCHROCK, V. E. & PETERSON, P. F. 1997 Rayleigh–Taylor instability of cylindrical jets with radial motion. *Nucl. Engng Des.* **177**, 121–129.

CHEW, J. W. 1996 Analysis of the oil film on the inside surface of an aero-enginer bearing chamber housing. *Tech. Rep.* 96-GT-300. ASME, International Gas Turbine and Aeroengine Congress & Exhibition, pp. 1–8.

DÁVALOS-OROZCO, L. A. 1993 Rayleigh–Taylor instability of two superposed fluids under imposed horizontal and parallel rotation and magnetic fields. *Fluid Dyn. Res.* **12**, 243–257.

DÁVALOS-OROZCO, L. A. 1996*a* Rayleigh–Taylor instability of a two-fluid layer under a general rotation field and a horizontal magnetic field. *Astrophys. Space Sci.* **243**, 291–313.

DÁVALOS-OROZCO, L. A. 1996*b* Rayleigh–Taylor stability of a two-fluid system under a general rotation field. *Dyn. Atmos. Oceans* **23**, 247–255.

DÁVALOS-OROZCO, L. A. & AGUILAR-ROSAS, J. E. 1989*a* Rayleigh–Taylor instability of a continuously stratified fluid under a general rotation field. *Phys. Fluids* A **1** (7), 1192–1199.

DÁVALOS-OROZCO, L. A. & AGUILAR-ROSAS, J. E. 1989*b* Rayleigh–Taylor instability of a continuously stratified magnetofluid under a general rotation field. *Phys. Fluids* A **1** (9), 1600–1602.

DÁVALOS-OROZCO, L. A. & VÁZQUEZ-LUIS, E. 2003 Instability of the interface between two inviscid fluids inside a rotating annulus in the absence of gravity. *Phys. Fluids* **15** (9), 2728–2739.

DESHPANDE, S. S., ANUMOLU, L. & TRUJILLO, M. F. 2012 Evaluating the performance of the two-phase flow solver interfoam. *Comput. Sci. Disc.* **5**, 014016.

GARCÍA-SENZ, D., CABEZON, R. M. & DOMÍNGUEZ, I. 2018 Surface and core detonations in rotating white dwarfs. *Astrophys. J.* **862** (1), 27.

HART, R. W. 1981 Generalized scalar potentials for linearized three-dimensional flows with vorticity. *Phys. Fluids* **24** (8), 1418.

HOCKING, L. M. 1960 The stability of a rigidly rotating column of liquid. *Mathematika* **6**, 25–32.

HOCKING, L. M. & MICHAEL, D. H. 1959 The stability of a column of rotating liquid. *Mathematika* **6**, 25–32.

JOHNSON, R. E. 1988 Steady-state coating flows inside a rotating horizontal cylinder. *J. Fluid Mech.* **190**, 321–342.

JOSEPH, D. D., RENARDY, Y., RENARDY, M. & NGUYEN, K. 1985 Stability of rigid motions and rollers in bicomponent flows of immiscible liquids. *J. Fluid Mech.* **153**, 151–165.

KUBITSCHEK, J. P. & WEIDMAN, P. D. 2007*a* The effect of viscosity on the stability of a uniformly rotating liquid column in zero gravity. *J. Fluid Mech.* **572**, 261–286.

KUBITSCHEK, J. P. & WEIDMAN, P. D. 2007*b* Helical instability of a rotating viscous liquid jet. *Phys. Fluids* **19**, 114108.

LAMB, H. 1932 *Hydrodynamics*, 6th edn. Cambridge University Press.

MILES, J. W. 1964 Free-surface oscillations in a slowly rotating fluid. *J. Fluid Mech.* **18** (2), 187.

RAYLEIGH, LORD 1879 On the stability of jets. *Proc. Lond. Math. Soc.* **9**, 4–13.

RAYLEIGH, LORD 1883 Investigation of the character of the equilibrium of an incompressible heavy fluid of variable density. *Proc. Roy. Math. Soc.* **14**, 170.

RAYLEIGH, LORD 1892 On the instability of a cylinder of viscous liquid under capillary force. *Phil. Mag.* **34**, 145–154.

SCASE, M. M., BALDWIN, K. A. & HILL, R. J. A. 2017*a* Magnetically induced rotating Rayleigh–Taylor instability. *J. Vis. Exp.* **121**, e55088.

https://doi.org/10.1017/jfm.2020.842 Published online by Cambridge University Press

SCASE, M. M., BALDWIN, K. A. & HILL, R. J. A. 2017*b* Rotating Rayleigh–Taylor instability. *Phys. Rev. Fluids* **2**, 024801.

SCASE, M. M., BALDWIN, K. A. & HILL, R. J. A. 2020 Magnetically induced Rayleigh–Taylor instability under rotation: comparison of experimental and theoretical results. *Phys. Rev.* E **102**, 043101.

SCASE, M. M. & HILL, R. J. A. 2018 Centrifugally forced Rayleigh–Taylor instability. *J. Fluid Mech.* **852**, 543–577.

TAO, J. J., HE, X. T., YE, W. H. & BUSSE, F. H. 2013 Nonlinear Rayleigh–Taylor instability of rotating inviscid fluids. *Phys. Rev.* E **87**, 013001.

TAYLOR, G. I. 1950 The instability of fluid surfaces when accelerated in a direction perpendicular to their planes. I. *Proc. R. Soc. Lond.* A **201**, 192.

WEIDMAN, P. D. 1994 Stability criteria for two immiscible fluids rotating in zero gravity. *Méch. Appl.* **39**, 481–496.

WEIDMAN, P. D., GOTO, M. & FRIDBERG, A. 1997 On the instability of inviscid, rigidly rotating immiscible fluids in zero gravity. *Z. Angew. Math. Phys.* **48**, 921–950.

WELLER, H. G., TABOR, G., JASAK, H. & FUREBY, C. 1998 A tensorial approach to computational continuum mechanics using object-oriented techniques. *J. Comp. Phys.* **12** (6), 620–631.

ZHOU, Y. 2017*a* Rayleigh–Taylor and Richtmyer–Meshkov instability induced flow, turbulence and mixing. I. *Phys. Rep.* **720–722**, 1–136.

ZHOU, Y. 2017*b* Rayleigh–Taylor and Richtmyer–Meshkov instability induced flow, turbulence and mixing. II. *Phys. Rep.* **723–725**, 1–160.

https://doi.org/10.1017/jfm.2020.842 Published online by Cambridge University Press